A review of 3D graphene materials for energy storage and conversion

WU Zi-yuan[1,2,†], XU Chi-wei[2,†], ZENG Jin-jue[2], JIANG Xiang-fen[1,*], WANG Xue-bin[2,*]

(1. *State Key Laboratory of Mechanics and Control for Aerospace Structures*, *Key Laboratory for Intelligent Nano Materials and Devices of the Ministry of Education*, *College of Material Science and Technology*, *Nanjing University of Aeronautics and Astronautics*, *Nanjing* 210016, *China*;
2. *National Laboratory of Solid State Microstructures (NLSSM)*, *Collaborative Innovation Center of Advanced Microstructures*, *Frontiers Science Center for Critical Earth Material Cycling*, *Jiangsu Key Laboratory of Artificial Functional Materials*, *College of Engineering and Applied Sciences*, *Nanjing University*, *Nanjing* 210093, *China*)

Abstract: Three-dimensional (3D) graphene monoliths are a new carbon material, that has tremendous potential in the fields of energy conversion and storage. They can solve the limitations of two-dimensional (2D) graphene sheets, including interlayer restacking, high contact resistance, and insufficient pore accessibility. By constructing interconnected porous networks, 3D graphenes not only retain the intrinsic advantages of 2D graphene sheets, such as high specific surface area, excellent electrical and thermal conductivities, good mechanical properties, and outstanding chemical stability, but also enable efficient mass transport of external fluid species. We summarize the fabrication methods for 3D graphenes, with a particular focus on their applications in energy-related systems. Techniques including chemical reduction assembly, chemical vapor deposition, 3D printing, chemical blowing, and zinc-tiered pyrolysis have been developed to change their pore structure and elemental composition, and ways in which they can be integrated with functional components. In terms of energy conversion and storage, they have found broad use in buffering mechanical impacts, suppressing noise, photothermal conversion, electromagnetic shielding and absorption. They have also been used in electrochemical energy systems such as supercapacitors, secondary batteries, and electrocatalysis. By reviewing recent progress in structural design and new applications, we also discuss the problems these materials face, including scalable fabrication and precise pore structure control, and possible new applications.

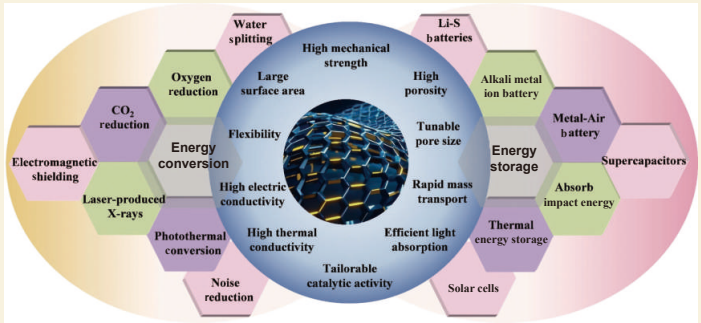

Key words: Graphene；3D network；Synthesis；Energy storage；Energy conversion

1 Introduction

Carbon is one of the basic elements in the world, its versatility is indispensable for the mass circle in nature as well as the progress of modern technology. The groundbreaking isolation of graphene-a 2D honeycomb lattice of sp^2-bonded carbon atoms-by Geim and Novoselov's team in 2004 marked a milestone in materials science[1]. This material theoretically has unparalleled characteristics: ultrahigh surface area (~ 2630 m^2 g^{-1}), exceptional charge mobility (>200 000 cm^2 V^{-1} s^{-1})[2–3], superior thermal conductivity (~ 5000 W m^{-1} K^{-1})[4], strong mechanical strength (with a Young's modulus of ~ 1 TPa)[5], and remarkable chemical stability. Graphene continues to revolutionize materials research through its unique 2D quantum behavior, including phenomena like the ambipolar field effect[1], quantum Hall effect[6–8], giant intrinsic carrier mobility , high sensitivity to external charge[9], among others. Furthermore, recent advances in synthesis methodologies have significantly enhanced production efficiency, enabling cost-effective fabrication and industrial-scale implementation of graphene-based technologies[10,13]. Endowed with a di-

Received: February 28, 2025
Revised: April 30, 2025
Accepted: April 30, 2025

verse array of attributes, graphene materials have found broadened applications, particularly in advancing energy storage and environmental conservation technlogies[14–16]. Nonetheless, the robust π-π stacking and van der Waals forces inherent between graphene sheets instigate significant aggregation, thereby drastically diminishing its key properties. As a consequence, vital characteristics such as its accessible specific surface area and catalytic active sites are substantially diminished, leading to a dearth of contiguous channels imperative for ion mobility. Meanwhile, the 2D stance of graphene has met challenges in energy storage and conversion devices, especially in large-scale 3D devices[17–19].

Given this context, researchers have begun to explore another dimension of graphene: 3D graphene. It is actualized by formulating a 3D porous configuration, which mitigates the re-stacking of graphene layers, while preserving the distinct 2D physical and chemical attributes inherent to graphene constituents[20–21]. Till date, various 3D porous graphene architectures have been achieved, encompassing macroscopic graphene hydrogel[22], graphene foam[23], graphene sponge[24], micrometric flower-like graphene[25], porous graphene structure[26–27], and strutted graphene[28], among others. There are two typical pathways for constructing 3D graphene materials: assembly of chemically exfoliated GO sheets[29] and CVD method[30]. The former is better suited for scale-up, but the resulting graphene often suffers from low mechanical strength, poor electric conductivity, and inferior interconnectivity of pore channels and graphene sheets. Conversely, the CVD technique renders high-quality 3D graphene with desired attributes for efficient energy devices, but its cost and complexity cast shadows on its scalability. In addition to these strategies, laser casting and 3D printing technology has been applied to prepare 3D graphene in recent years. The evolution of such 3D graphene constructs has vastly expanded the application sphere of graphene materials[12,31]. Now, they have permeated a myriad of fields, from energy storage devices like supercapacitors[32] and batteries[33] to solar cells[34], sensors, conductors[35], solar-thermal conversion facilities[36], thermal management devices[37], catalysis[38–39], electromagnetic interference shielding[40–41] and beyond.

3D graphene materials obtained through diverse methodologies exhibit distinctively different properties, imparting various features to each application. The realization of the full potential of these applications necessitates a deeper comprehension of the correlation between the material's unique properties and its performance. Among energy storage devices, the hierarchical porosity and high contact area of 3D graphene satisfy the requirement for accommodate substantial charge storage as well as facilitate efficient ion and electron transport during charge-discharge cycles[19]. Meanwhile, superior conductivity and robust graphene 3D network contribute to a significant improvement in performance and applicability[34]. In the sphere of electrocatalysis applications, noble metals catalysts are not ideal due to high costs, despite being commonly used. Here, 3D graphene fills the gap, with its abundant active sites, high conductivity and low cost[42]. And 3D graphene offer a distinctive combination of light weight, flexibility, broadband and low load, which is conducive to the improvement of microwave absorption performance[41]. Besides, benefiting from the high porosity and low density, 3D graphene material is a light-but-strong structural supporter and excellent elastomer with excellent impact resistance[43]. Moreover, 3D graphene can integrate with other active materials, leading to optimized corresponding performance in specific applications. The effects of such integration can be seen in several ways: (1) The polarization of electron density at carbon-heteroatom bonds, brought about by heteroatom doping into the honeycomb lattices of 3D graphene, facilitating opportunities for modifying the sp^2 bonding state, which would open the intrinsic electronic structure and generate many active sites[44]. (2) An expansion of surface area and the formation of extensive ion/mass transport pathways, resulting from the introduction of porous structures into graphene nanosheets of 3D graphene, in

some cases improving their (chemical/mechanical/thermal) stability[27]. (3) An increased overall conductivity and stabilize the 3D interconnected configuration, introduced by the collaboration with conductive polymers[45]. (4) Surface modification of graphene with other functional components (metal sulfide, metal oxide, single metal atoms, etc.) can not only modulate its surface and interface behaviors but also induce new functions via synergetic effects of different species[46–48].

So far, several excellent articles have provided comprehensive reviews regarding 3D graphene materials from various perspectives[19–21,38–40]. However, the latest pertinent reviews primarily center on 3D graphene-based composite materials in specific application domains. As shown in Fig. 1, this review summarizes the latest advances of 3D graphene in the fields of energy conversion (e.g., electrocatalysis and photothermal conversion), energy absorption (e.g., absorbing impact energy and electromagnetic waves), and energy storage (e.g., rechargeable batteries, supercapacitors and heat storage). This work begins with the latest understanding of 3D graphene structure and properties, as well as a comparison between various advanced graphene preparation methodologies. Subsequently, we delve into the applications of the 3D graphene from generic electrochemical performances to environmental and industrial applications. The ultimate goal of this article is to aid readers in acquiring a deeper comprehension of the latest developments in 3D graphene, and in identifying the future challenges and directions in this domain.

2 Structure and properties of 3D graphene materials

2.1 Structure of 3D graphene materials

The structure of 3D graphene could be seen as a network of 2D graphene sheets bonded together to create nodes and struts, maintaining adjacency while leaving void spaces called pores. Essentially, 3D graphene exploits the merits of 2D graphene sheets, extending these properties into the third dimension. Based on structural length scales, 3D graphene architectures are classified into two categories: (1) Macroscopic 3D graphene materials (embodied in forms such as foams[23], sponges[24], aerogels[22], films[49], fibers[25] and millimeter spheres[50]) with dimensions surpassing 100 μm; (2) Microscopic 3D graphene materials, despite being powdered, exhibit intricate 3D structures at micro or nano scales[21]. Macroscopic 3D graphene typically boasts low mass density and high specific surface area, making it potentially robust for various free-standing or binder-free applications[12]. On the other hand, the 3D microscopic graphene nanostructures are fashioned by the fusion of numerous hexatomic-ring-containing monomers. This powdered form of 3D graphene can serve a breadth of applications similar to macroscopic graphene monoliths, once a suitable shaping procedure is undertaken[11].

2.2 Properties of 3D graphene materials

The excellent electrical conductivity of graphene

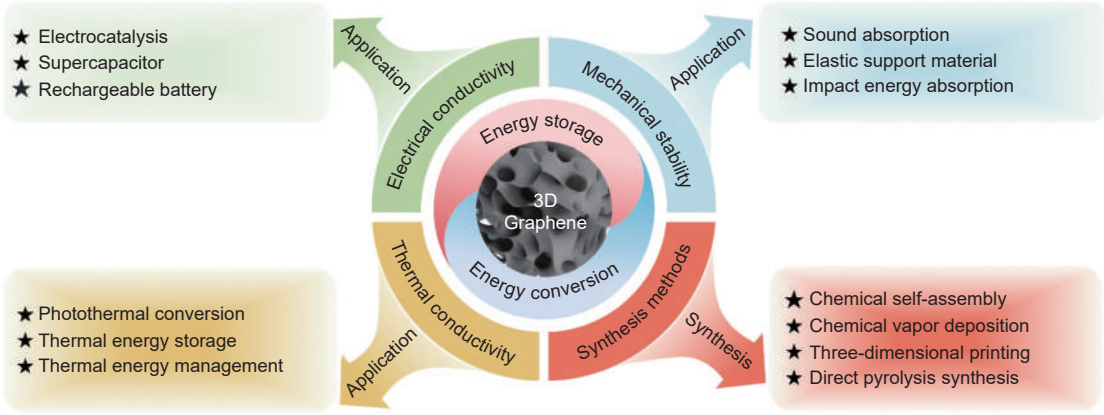

Fig. 1 General diagram of the features and applications of the 3D graphene

is inherited by its 3D counterparts, due to which the 3D graphene materials maintains Dirac fermion properties (Fig. 2a) with superior electron mobility. Photoemission spectroscopy analysis confirms the preserved linear electronic density of states near the Fermi level in these 3D graphene materials, the same as the signature Dirac cone features observed in conventional 2D graphene (Fig. 2b, c). Notably, the 3D architecture with isotropic porosity and randomly oriented graphene sheets demonstrates angle-independent photoemission characteristics (Fig. 2d), in striking contrast to the anisotropic behavior of conventional 2D graphene[51]. Remarkably, the "unified" 3D graphene networks, where carbon atoms are continuously connected through chemical bonds, can well preserve the 2D electronic properties of graphene with massless Dirac fermions[26]. Their electric conductivity significantly are higher than those of "jointed" 3D graphene architectures, where many independent graphene pieces are interconnected via van der Waals forces. To illustrate this, graphene foam synthesized by Ni-foam-based CVD demonstrates a conductivity of 10 S cm^{-1} when incorporated into a poly(dimethylsiloxane) (PDMS) composite[52]. Additionally, a nanoporous graphene monolith, templated with SiO_2, achieves a conductivity of 32 S cm^{-1}[53].

The 3D graphene structure is distinguished by its robustness and continuity, while also being lightweight due to its primarily porous structure. This results in an impressively high specific strength (the ratio of strength to density) that surpasses that of numerous advanced materials. This is evidenced in the production of aluminum-based graphene/metal metamaterial composites through electron beam evaporation[54]. The outstanding rigidity and superelasticity of the 3D graphene foam was utilized in composites to demonstrate an exceptional spring constant of approximately 15 N m^{-1} and a recoverable deform-

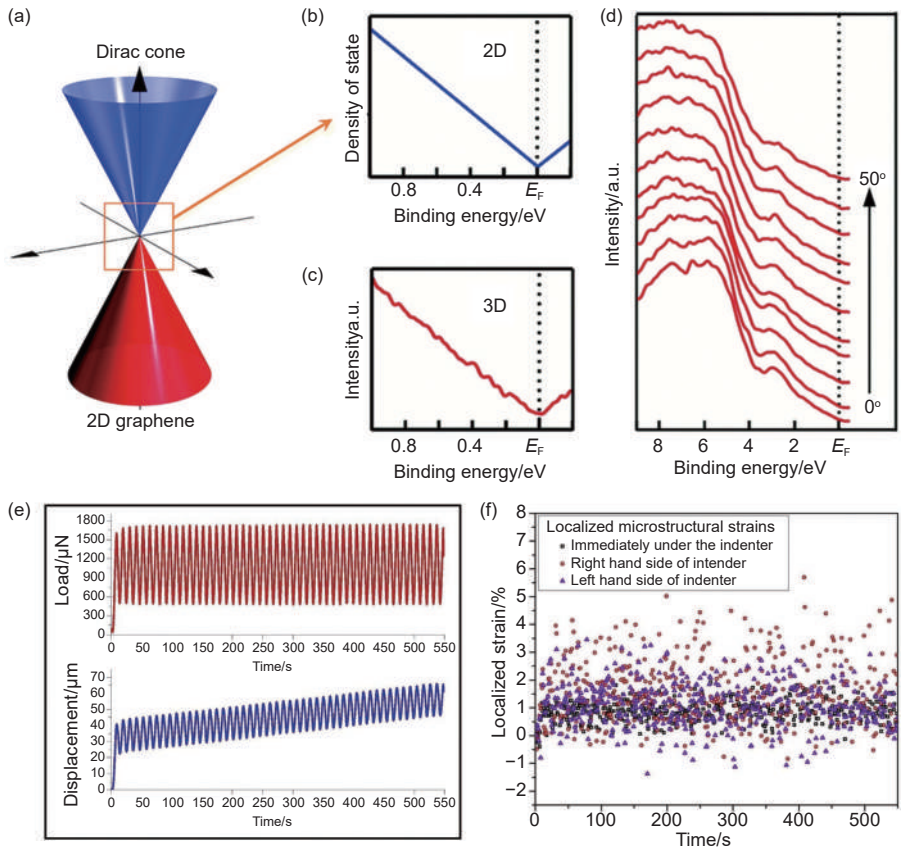

Fig. 2 (a) Conventional 2D graphene Dirac cone dispersion. Electronic DOS around the Dirac point in (b) 2D and (c) 3D graphene materials. (d) Angle-resolved PES spectra in a wider energy region for 3D nanoporous graphene (Reproduced with permission, Copyright 2022, John Wiley and Sons[19]). (e) Cyclic loading-unloading profile and the corresponding displacement response during nanoindentation fatigue testing. (f) Evolution of local strain values during the course of 50 fatigue cycles (Reproduced with permission, Copyright 2018, Elsevier[54])

ation exceeding 70% (Fig. 2e, f). The mechanical strength and modulus can differ across various 3D graphene structures, depending on the porous geometry and the quality of the graphene sheets. Li et al.[55] explored the uniaxial in-plane compressive properties of honeycomb 3D (h3D), triangle-like 3D (t3D), and non-equilateral hexagon 3D (nh3D) graphene using a combination of molecular dynamics (MD) simulations and continuum modeling. They discovered that the graphene sidewalls of h3D graphene tend to undergo buckling deformations, resulting in significant locking strain in h3D graphene. The t3D and nh3D graphene exhibit higher plateau stress due to their unique configurations. Additionally, to investigate the impact of graphene thickness and length distribution on the mechanical properties of graphene networks, molecular dynamics simulations were performed based on a coarse-grained graphene model by Bao et al.[56]. The results show that monolayer graphene is highly flexible and prone to crumpling, which enhances the interactions between graphene sheets. Compared with the graphene networks with different structures, those with a Gaussian distribution of graphene lengths exhibit superior compressive strength due to the increased density.

Notably, 2D graphene sheets exhibit a decreased specific surface area during processing due to the inevitable restacking. In fact, this is substantially inferior to the theoretical surface area of 2630 m^2 g^{-1} for monolayer graphene. In contrast, the 3D graphene effectively avoids the restacking and hence can offer a larger specific surface area. The high specific surface area facilitates superior interaction interfaces for various applications, such as energy storage, catalysis, and gas adsorption, among others. This characteristic, coupled with the modulation of porosity, permits the tailoring of sorption characteristics to match the required application. A dynamic assembly method, induced by ion-crosslinking, was employed to modulate the microstructure of a 3D GO framework[57]. This was achieved by varying the concentration of GO, thereby mitigating GO nanosheets aggregation and restacking during fabrication. The 3D GO framework after optimization adsorbent demonstrated a CO_2 adsorption capacity of 2.24 mmol g^{-1} at ambient pressure and temperature, coupled with notable operational stability.

Furthermore, 3D graphene displays markedly high thermal conductivity, a characteristics inherited from 2D graphene, which is typically ~ 5000 W m^{-1} K^{-1} at room temperature. These excellent heat-dissipating capabilities present a solution to the overheating problems inherent in modern electronics. The natural wood fibers are used as the template and coated with graphene nanoplates to obtained biocomposite consisting of highly efficient 3D fibrous “tracks” for heat transmission[58]. The biocomposite exhibits extremely high thermal conductivity of 134 W m^{-1} K^{-1} comparable to many metals. Moreover, Bo et al.[59] proposed the use of a 3D graphene structure equipped with covalently-bonded nanofins as a filler for aqueous media. The thermal conductivity and its enhancement efficiency of aqueous medium can be as high as 2.61 W m^{-1} K^{-1} and 1300%, respectively.

Finally, in contrast to 2D graphene, the continuously porous 3D graphene features abundant curvatures and curvature gradients due to its unique spatial topology and continuity. This leads to the emergence of topological defects, a phenomenon confirmed through high-resolution transmission electron microscopy (HRTEM) in nanoporous graphene samples (Fig. 3a-c)[26,60]. Notably, Tanabe et al.[61] demonstrated that the ambipolar electronic states of Dirac fermions are fundamentally preserved in 3D graphene nanostructures with a curvature radius of 25–50 nm in 3D nanoporous graphene (Fig. 3d, 4e). Additionally, they found that the 3D curvature effectively dampens the slope of the linear density of states of Dirac fermions near the Fermi level. Importantly, the 3D curvature can be exploit to control the backscattering-inhibited electrical transport of Dirac fermions and augment electron-electron interaction and electron localization. Furthermore, Tanabe et al.[62] also found that the dual nature of electronic states, resulting from the synergetic effect of nitrogen doping and 3D curvature of graphene, underpins the en-

hanced electrocatalysis, light absorption, and molecular adsorption capacities of nitrogen-doped 3D graphene (Fig. 3f). As a result, nanoscale curvature offers a novel degree of freedom to modify graphene's electrical properties to achieve new functionalities.

3 Fabrication methods for 3D graphene materials

As shown in Fig. 4, significant efforts in the past decade have focused on developing 3D graphene materials while maintaining the 2D properties of graphene[22,28,52,63–68]. The most commonly used methods for this purpose include CVD, GO assembly, 3D printing, and direct pyrolysis synthesis. The Table 1 compares the performance parameters and application scenarios of these synthesis methods.

3.1 CVD

Among the various techniques developed for fabricating 3D graphene frameworks, CVD is widely used to produce high-quality graphene. In this method, metal substrates are typically employed as catalysts. At high temperature, carbon-containing precursors undergo pyrolysis and deposit onto the substrate. After removing the substrate, 3D graphene with diverse structures and properties can be achieved.

To address the high inter-sheet junction contact resistance in chemically derived 3D graphene, Chen et al.[52] used CVD to develop graphene foams (GFs). As show in Fig. 5a, porous nickel (Ni) foam and methane (CH_4) were selected as the scaffold and carbon source, respectively. To protect the 3D graphene network, a thin layer of poly(methyl methacrylate) (PMMA) was coated on the graphene-Ni foam surface. After etching the Ni template and PMMA layer, a graphene foam consisting of an interconnected, flexible network of graphene was successfully obtained. Moreover, the number of graphene layers, specific surface area, and density of GFs could be controlled

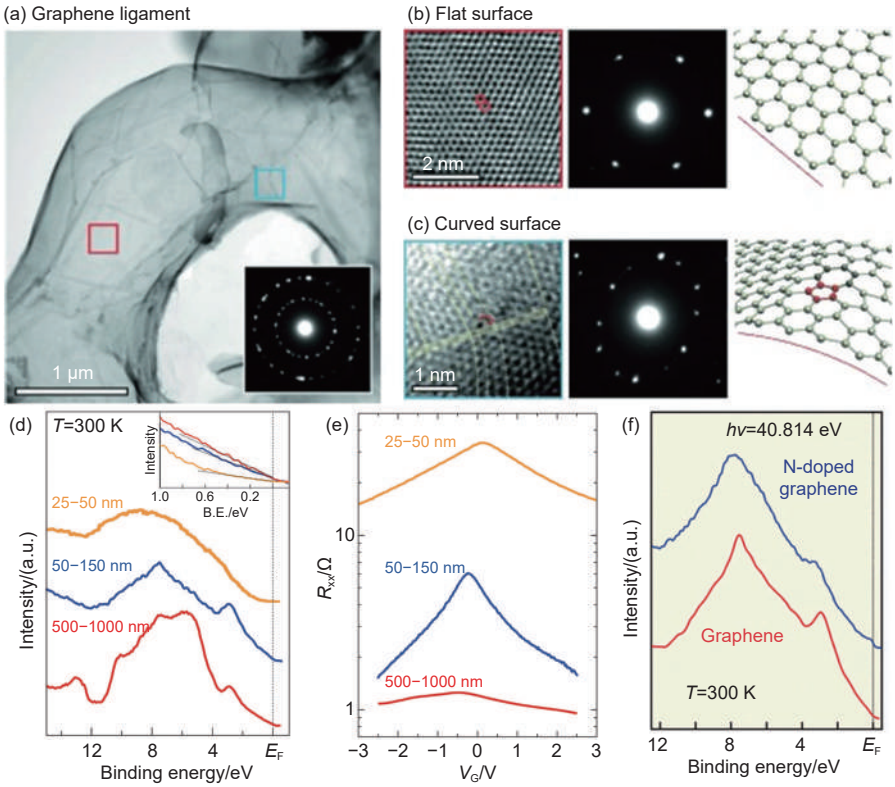

Fig. 3 (a-c) Low-magnification and high-resolution TEM images, selected area electron diffraction patterns, and atomic models of 3D graphene, showing high-quality graphene lattices with observable geometric defects in the heavily curved regions. (d) Angle-integrated photoemission spectra (PES) of 3D nanoporous graphene with different curvature radius. The inset shows the angle-integrated PES near the Fermi level. (e) Longitudinal resistance against the gate voltage for the 3D nanoporous graphene-based electric double-layer transistor at room temperature (Reproduced with permission, Copyright 2020, John Wiley and Sons[61]). (f) Angle-integrated PES of N-doped 3D graphene and pristine 3D graphene (Reproduced with permission, Copyright 2022, John Wiley and Sons[62])

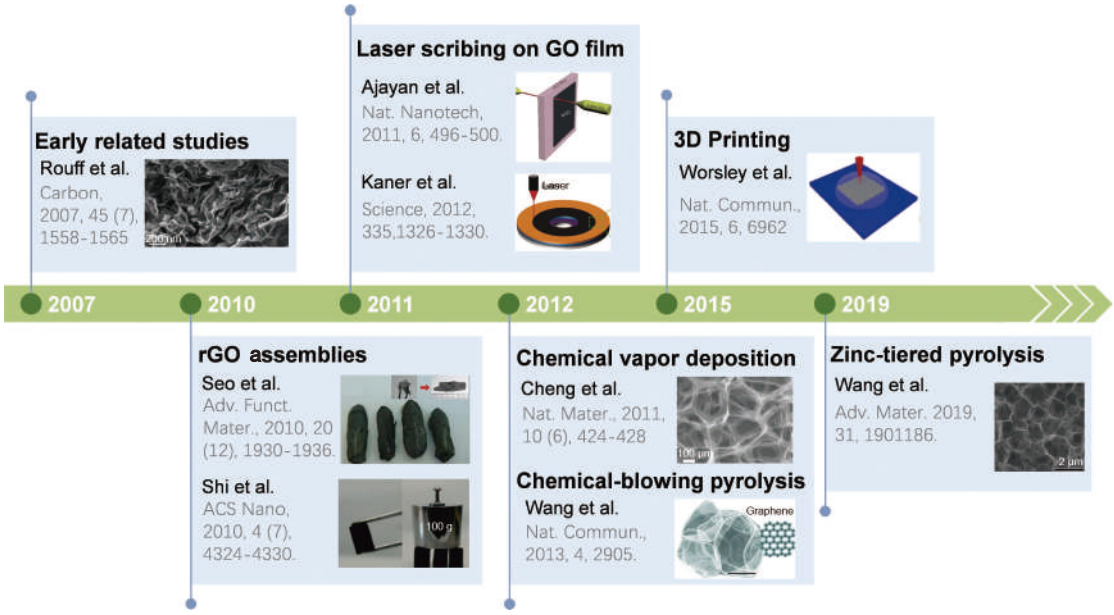

Fig. 4 Milestones for the development of 3D graphene materials

Table 1 Comparison of preparation methods of 3D graphene

Method	Advantages	Disadvantages	Application scenarios	Performance parameters
CVD	High-quality graphene layers; Controllable structure	Requires high temperature and gas environment	High-performance electronic devices; Manufacturing of high-quality graphene films	High conductivity; Excellent electron mobility; Controllable thickness and structure
GO self-assembly	Simple operation and low cost; Performed at room temperature; Suitable for large-area preparation	Relatively low graphene quality; Difficult to precisely control the self-assembly process	Sensors; Environmental monitoring; Conductive films	Relatively low conductivity
3D printing	Complex 3D structures; High controllability; Suitable for different shapes	Slow printing speed and limited precision	Customized products; Sensors; Device prototypes	Lower conductivity
Direct pyrolysis synthesis	High-quality graphene layers; Controllable structure; In-situ sacrificial template	Complex equipment; Requires high temperature and gas environment	High-performance electronic devices; Manufacturing of high-quality graphene films	Higher conductivity

by adjusting the CH_4 concentration. A higher CH_4 concentration increases the number of graphene layers, which in turn significantly affects the specific surface area, density, and electrical conductivity of the GFs. For example, a GF produced with a CH_4 concentration of 0.7% has an ultra-low density of approximately 5 mg cm^{-3} and a high porosity of about 99.7%. This GF also exhibits a very high specific surface area of around 850 m^2 g^{-1} and an average of about 3 layers. The seamless and compact graphene sheets endow the GF/poly(dimethyl siloxane) composites with exceptional electrical conductivity of 10 S cm^{-1}, approximately 6 orders of magnitude higher than that of chemically derived graphene-based composites. A similar approach was pursued by Pan et al.[69], who substituted the Ni substrate with porous copper foil (Fig. 5b). Then the strain sensors with high sensitivity and large stretch are obtained.

Furthermore, Gao et al.[70] merged the dual strategies of 3D-network support and sandwiching design. Through an O_2/NH_3-mediated pyrolysis process of cellulose precursors, the pre-oxidation and ammonolysis reactions induced controlled spatial carbonization of cellulose molecular chains (Fig. 5c). This innovative methodology successfully transforms individual cellulose fibers into assemblies of ultrathin, interwoven graphene nanosheets, rather than forming conventional carbon fibers. Consequently, this enables direct conversion of cellulose paper into mechanically robust, porous carbon membranes exhibiting enhanced specific surface area and electrical conductivity (denoted as CP). When employed as a 3D network support to construct the hybrid CP@Fe_3O_4@RGO electrodes, the resulting lithium-ion batteries demonstrated exceptional cycling stability and remarkably improved capacity retention. Besides, 3D

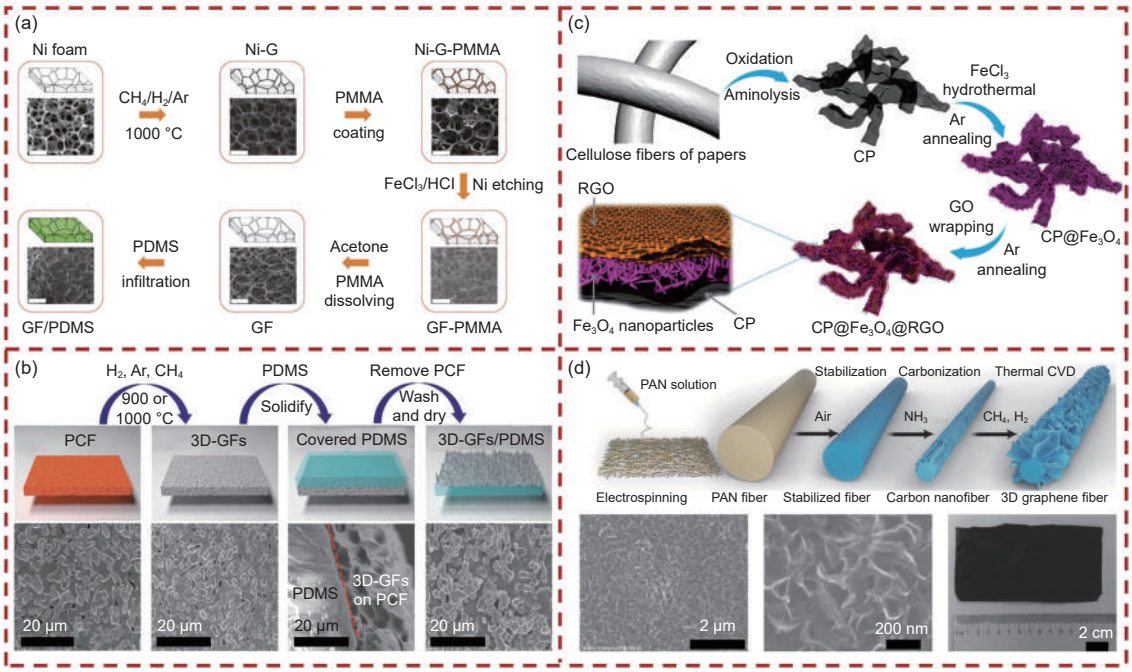

Fig. 5 (a) Synthesis of GF by CVD growth with a Ni foam template and integration with polydimethylsiloxane, and corresponding SEM images (Reproduced with permission, Copyright 2011, Springer Nature[52]). (b) Synthesis of 3D-GFs on PDMS, and corresponding SEM images (Reproduced with permission, Copyright 2018, John Wiley and Sons[69]). (c) Scheme of synthesis of CP and fabrication of CP@Fe_3O_4@RGO (Reproduced with permission, Copyright 2019, American Chemical Society[70]). (d) Schematic illustration of the preparation process and structure of the 3DGFs (Reproduced with permission, Copyright 2018, John Wiley and Sons[25])

graphene fibers with a novel 3D structure were developed by carbonizing electrospun polyacrylonitrile (PAN) fibers in ammonia (NH_3) and subsequently in-situ growing radially oriented graphene sheets (GSs) using thermal CVD (Fig. 5d)[25]. Notably, the growth of GSs depends on both temperature and CH_4 concentration. As temperature and CH_4 concentration increase, the growth rate, density and thickness of GSs also rise. These two factors are closely related, and at higher temperatures, the optimal CH_4 concentration range for GS growth shifts lower. For instance, at 1100 °C, the suitable CH_4 concentration range is 5%–20%. Exceeding this upper limit leads to the formation of continuous overcoatings rather than GSs. Finally, the GSs on the 3D graphene fibers are densely packed and interconnected, with fully exposed edges, leading to superior performance in various applications such as electrical conductivity, electromagnetic shielding, superhydrophobicity, and superoleophilicity.

3.2 GO chemical self-assembly

In addition to CVD-based methods, solution-based techniques that rely on the self-assembly of GO sheets into 3D frameworks offer another effective approach for fabricating 3D graphene. Typically, the hydrothermal method would be employed to promote the self-assembly of GO sheets into a 3D graphene structure. For instance, Xu et al.[22] prepared a self-assembled graphene hydrogel (SGH) using a simple one-step hydrothermal process. The SGH exhibited an electrical conductivity of up to 5×10^{-3} S cm^{-1} and demonstrated high specific capacitance (175 F g^{-1}) as a 3D supercapacitor electrode material in an aqueous electrolyte. Moreover, a 3D graphene framework with vertically aligned graphene sheets over a long range was synthesized using an antifreeze-assisted freezing method[71]. The self-supporting VA-GSM structure, which features continuous channels that facilitate water transport, high light absorption for effective photothermal conversion, and exceptional stability in harsh conditions, ensures highly efficient solar thermal conversion (Fig. 6a).

Apart from the abovementioned strategies, the use of sacrificial templates is another approach for preparing 3D graphene materials, allowing for precise control over the size, uniformity, and shape of the en-

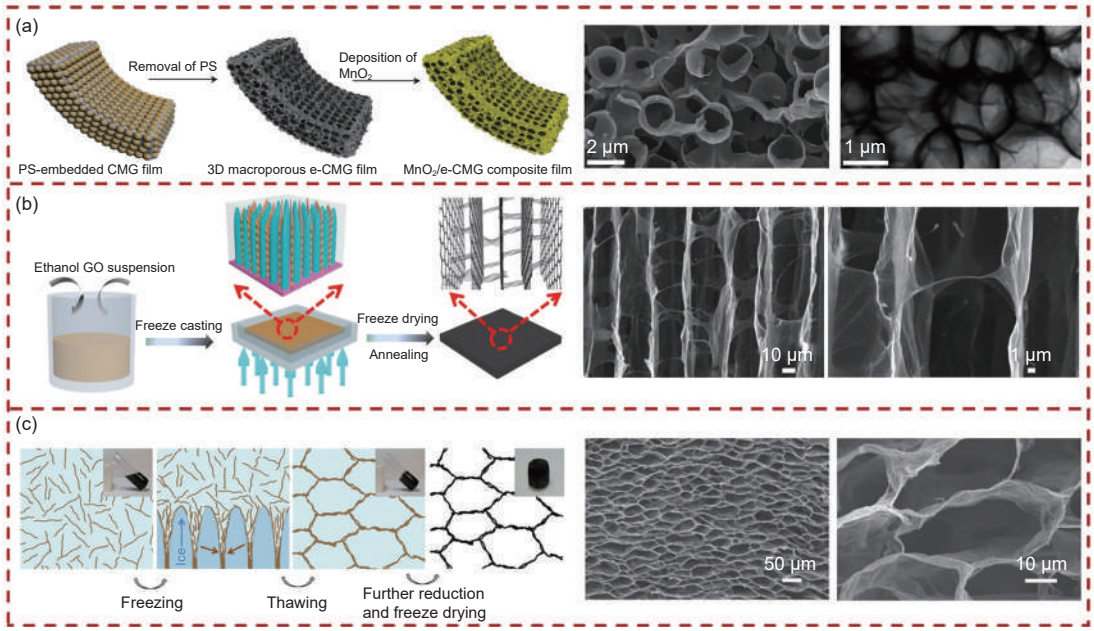

Fig. 6 (a) Schematic of the fabrication process of VA-GSM and SEM images of VA-GSM (Reproduced with permission, Copyright 2017, American Chemical Society[71]). (b)Schematic illustrating a procedure to fabricate MnO_2/e-CMG film and SEM images of e-CMG film (Reproduced with permission, Copyright 2012, American Chemical Society[72]). (c) SEM images and schematic showing the formation mechanism of the cork-like monolith by freeze casting (Reproduced with permission, Copyright 2012, Springer Nature[74])

tire framework. As shown in Fig. 6b, Choi et al.[72] developed a 3D macroporous structure composed of chemically modified graphene (CMG) by utilizing polystyrene colloidal particles as a sacrificial template. The resulting porous graphene structure, with a large surface area, facilitates fast ionic transport within the electrode while maintaining good electronic conductivity, thereby enhancing the electrochemical properties of MnO_2/e-CMG composite electrodes. Furthermore, ice crystals can serve as solid templates to shape the building blocks, offering a simple and effective self-assembly strategy for obtaining porous microstructures[73]. Qiu et al.[74] reported the preparation of ultralight and superelastic graphene-based cellular monoliths by combining graphene chemistry with ice physics. This biomimetic hierarchical structure provides the material with exceptionally high energy absorption and good electrical conductivity (Fig. 6c). The resulting elastomers can maintain structural integrity under loads exceeding 50 000 times their own weight and recover more than 80% of their original shape after compression.

3.3 3D printing

Compared to the methods previously discussed, the automated 3D printing technique offers a low-energy and efficient alternative for fabricating 3D graphene[75]. Moreover, 3D printing enables the construction of macroscopic structures with tailored porosity and specific hierarchical architectures, thanks to precise computer control[76]. For example, Ma et al.[77] fabricated a high-performance, shape-designable 3D graphene monolith using a 3D printing method with large-sized GO (LGO) fluid ink (Fig. 7a). The resulting 3D graphene exhibited high electrical conductivity (41.1 S m^{-1}), specific strength (10.7 × 10^3 N m^{-1} kg^{-1}), and compressibility (up to 80% compressive strain). In order to enhance printing accuracy, Chen et al.[78] developed printable GO inks by modifying the oxygen functional groups, enabling the printing of self-standing 3D GO aerogel microlattices (GOAL) with an ultra-high printing resolution of 70 μm. The high resolution of the printed GOAL tape improves performance and data readability when used as micro sensors or in robotic e-skin applications.

Apart from direct GO ink writing prepared 3D graphene, another commonly used approach involves printing a 3D template and then fabricating the 3D graphene on the template. For example, Fig. 7b show a 3D nitrogen-doped graphene (NG) foam prepared

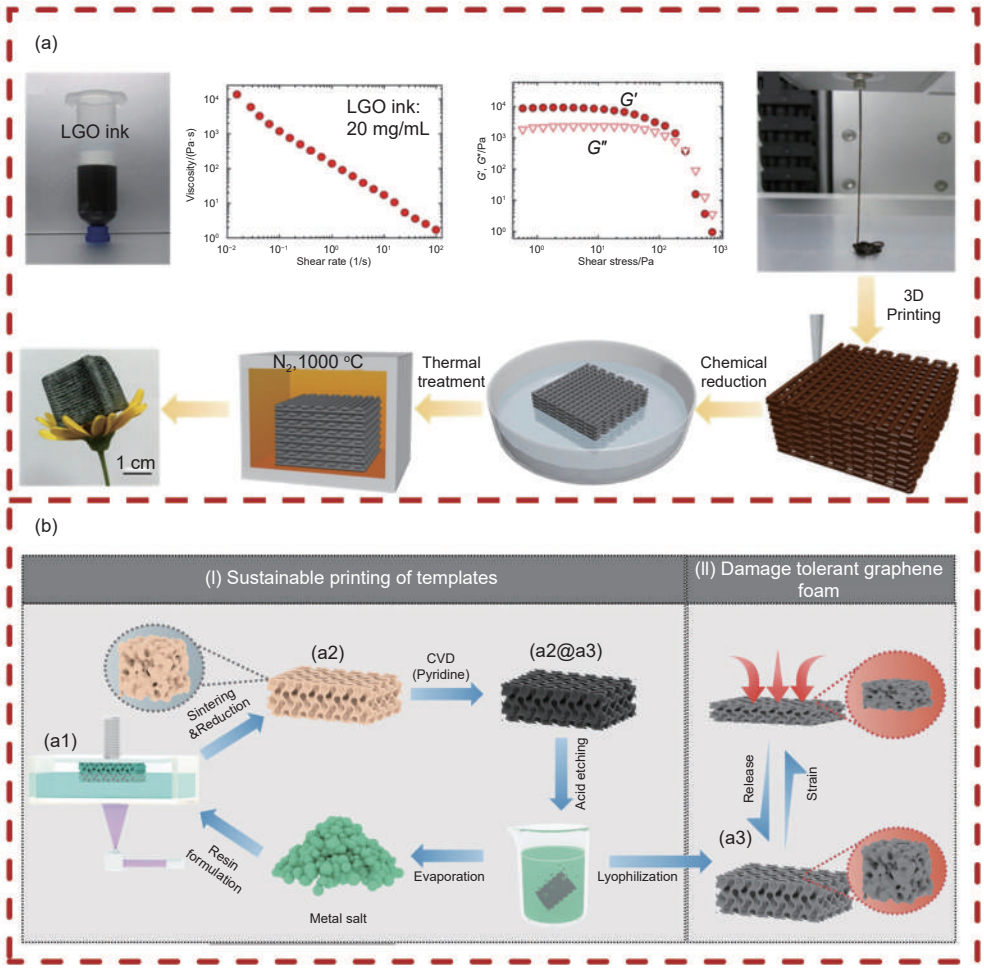

Fig. 7 (a) LGO ink properties and schematic diagram of the fabrication process (Reproduced with permission, Copyright 2019, Elsevier[77]). (b) Schematic diagram of the fabrication process of 3D metal templates and 3D NG foams (Reproduced with permission, Copyright 2023, John Wiley and Sons[79])

using 3D printed templates followed by template-directed CVD[79]. The resulting 3D graphene foam demonstrated nearly complete strain recovery under loads of up to 62 500 times its own weight and fast charge carrier transport (5 S cm^{-1}). Similarly, Zhang et al.[80] constructed 3D graphene lattices (GLs) using a combination of 3D stereolithography printed hollow polymer templates, hydrothermal processing, and freeze-drying strategies. The porous structure of GLs exhibited a well-ordered, honeycomb-like microstructure and possessed multifunctional properties, including robustness structural, elastic deformation, high electrical conductivity, significant Joule heating effect, and substantial capacitance for organic solvent absorption.

3.4 Others

Apart from the methods mentioned above, several alternative synthesis techniques have been explored for the fabrication of 3D graphene materials, including laser-induced method[67], aerosolization method[81], and direct pyrolysis synthesis (including sugar-blowing approach and zinc-tiered pyrolysis) (Fig. 8a, b)[28], etc. Using the sugar-blowing method, Wang et al. synthesized a 3D graphene bubble network from a polymer precursor. The corresponding network consisted of mono- or few-layered graphitic membranes that are tightly bonded, rigidly fixed, and supported by micrometer-scale graphitic struts. This unique structure ensured strong interconnectivity, efficient electron/phonon transport, a large accessible surface area, and enhanced mechanical properties. Besides, our group has reported a zinc-assisted solid-state pyrolysis method to produce high-quality 3D graphene (Fig. 8b)[68]. In this approach, glucose and zinc powders are compacted into a glucose-zinc ingot, which is then heated to directly form a monolithic,

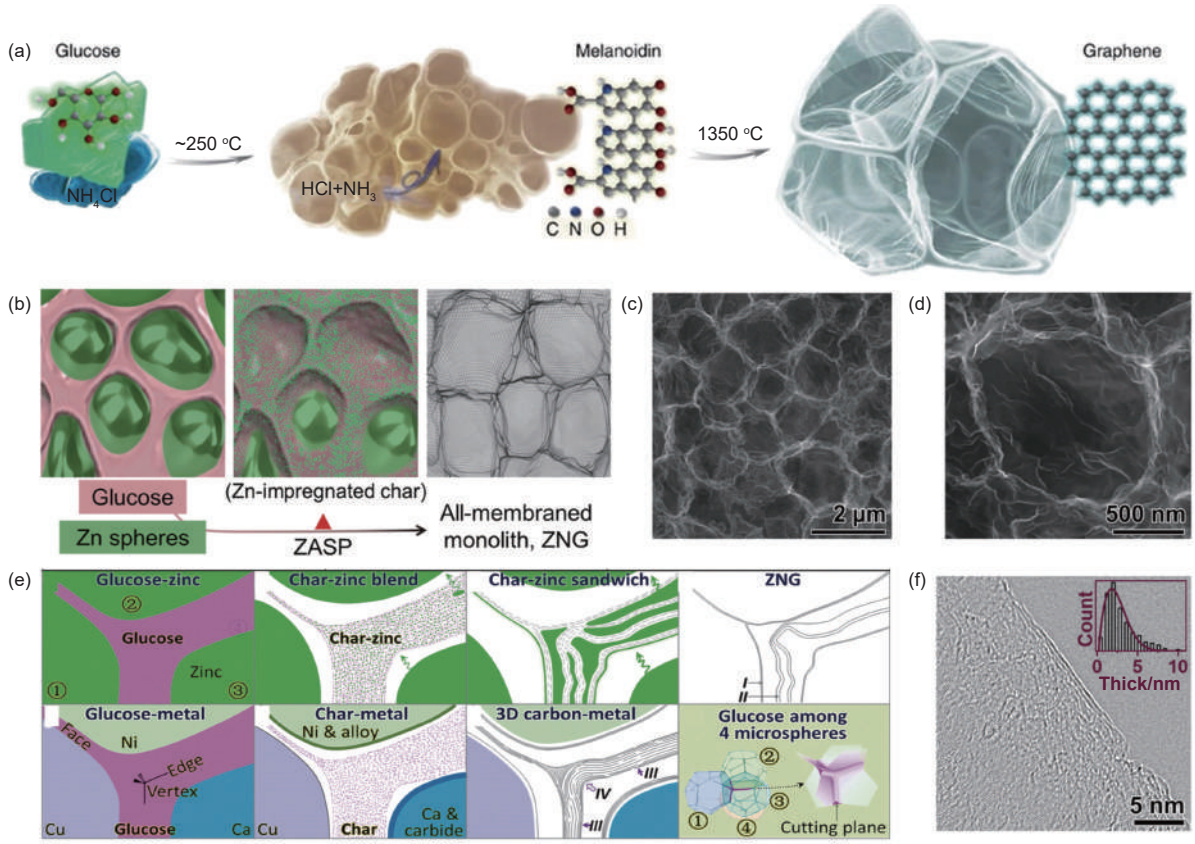

Fig. 8 (a) Growth process and structural regulation of sugar-blowing production (Reproduced with permission, Copyright 2013, Springer Nature[28]). (b) Scheme of ZASP route undergoing a char-zinc intermediate. (c, d) SEM images of ZNG. (e) Mechanism of zinc prompted pyrolysis and zinc tiering effect. (f) HRTEM image of an individual graphene membrane (Reproduced with permission, Copyright 2019, John Wiley and Sons[68])

well-graphitized 3D graphene structure (Fig. 8c, d). During the heating process, zinc impregnates and delaminates glucose char into multiple membranes while also catalyzing the carbonization and graphitization processes (Fig. 8e). The resulting 3D graphene network consists of chemically and morphologically pure graphene membranes (Fig. 8f). Owing to the unique structures, this material exhibits exceptional surface area, stability and conductivity.

4 Mechanical and acoustical energy-related applications based on 3D graphene

4.1 3D graphene as an elastic material to absorb impact energy

Thanks to its high porosity and low density, 3D graphene material serves as a lightweight yet strong structural support and an excellent elastomer, offering remarkable impact resistance. Inspired by the hierarchical structure of natural cork, Qiu et al.[74] developed ultra-light and highly elastic graphene monomer cells using the ice-physical template method. These materials are capable of withstanding loads exceeding 50 000 times their own weight while recovering more than 80% of their original shape after compression. The biomimetic hierarchical structure also imparts exceptional energy absorption capacity and good electrical conductivity to these elastomers. However, their limited macroscale has restricted their practical applications. To overcome this limitation, Yang et al.[82] introduced a straightforward wet-press assembly technique to create ultrastrong, superelastic graphene aerogels with an unlimited macroscale, based on a novel superplastic air-dryable graphene hydrogel (SAGH). Specifically, the SAGH was first prepared through a dual-template sol-gel method, resulting in an isotropic, open-cell, highly porous microstructure (Fig. 9a). By pressing and air-drying countless SAGH "bricks," a wet-press assembled graphene

aerogel (WAGA) “wall” was formed, with a highly oriented, dense, multi-arch structure (Fig. 9b, c). As shown in Fig. 9d, the WAGA demonstrates exceptional compressive strength (47 MPa), and super elasticity (>97% strain).

To broaden the applications of 3D graphene elastomers, combining them with other structural materials is an effective strategy. For instance, Nautiyal et al.[54] reported a 3D macroporous graphene foam-based mechanical (Al) metamaterial that is ultra-light, stiff, and resistant to fatigue. The interconnected network of branches in the material allowed for long-distance stress transfer. So, the material demonstrated high fatigue resistance, with over 98% displacement recovery after each loading/unloading cycle. The material exhibited 2 strengthening mechanisms: stress transfer from the aluminum layer to the graphene scaffold enhanced the overall load-bearing capacity, while the aluminum deposit on the graphene foam acted as a structural backbone to prevent brittle failure. Furthermore, PDA-modified reduced graphene oxide (PDA-rGO) was applied to the skeleton of nickel foam to examine its mechanical properties and vibration damping performance[83]. Mechanical tests revealed that the coating led to a 240% increase in compressive modulus and a 59% increase in yield strength. In dynamic mechanical analysis (DMA) tests, the loss factor of nickel foam coated with PDA-rGO increased by 170%, demonstrating excellent stability with rising temperature, which confirms the reliability of the enhancement in harsh conditions. To explore the impact energy absorption mechanism of 3D graphene further, Zhang et al.[84] designed a 3D graphene origami (GOri)-reinforced copper nanocomposite and studied

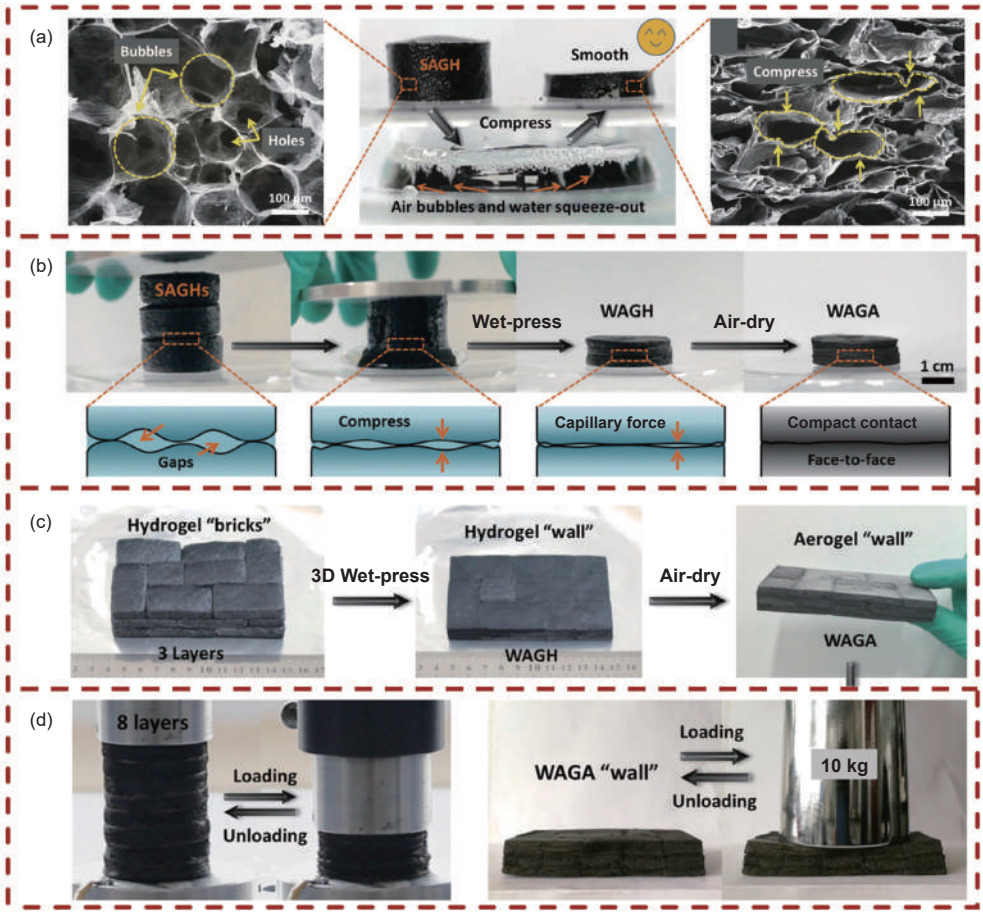

Fig. 9 (a) SEM images of the cross-section of SAGH before and after compression. (b) Wet-Press assembly process of WAGA prepared by 3 SAGHs after air-drying and schematic illustration of the compact interface formation process caused by wet-press and capillary force. (c) Wet-press assembly process of huge WAGA “wall” prepared by SAGH “bricks” after air-drying. (d) Uniaxial compression and recovery process of the 8-layer WAGA at 70% compressive strain; loading and unloading process of the WAGA “wall” by a 10 kg weight ((Reproduced with permission, Copyright 2019, John Wiley and Sons[82])

its wave propagation characteristics under high-velocity ballistic impact using molecular dynamics (MD) simulations. The study found that transforming the intrinsic 2D graphene into a 3D origami structure alleviated its brittleness. Embedding GOri in the copper matrix increased the out-of-plane wave propagation speed, thereby enhancing the dissipation of impact energy by promoting rapid dislocation propagation within the copper matrix during the early stages of impact.

4.2 3D graphene as noise reduction and sound absorption material

Noise pollution, recognized as one of the three major environmental pollutants, has become a significant threat to both human health and the global economy. As a result, the development of acoustic-absorbing materials is receiving more interest. However, currently many noise absorbers face limitations such as narrow range of sound absorption across a wide frequency range, excessive weight and thickness, poor moisture resistance, and instability under high temperatures[85].

Atomically thin 2D graphene sheets exhibit exceptional in-plane stiffness and significant out-of-plane elasticity, making them ideal for enhancing the mechanical resonance of nanomechanical devices. This remarkable resonance behavior of ultrathin graphene presents promising opportunities for the development of advanced acoustic absorption materials. When assembled into a 3D structure, graphene sheets form a highly porous, low-density material that is both lightweight and structurally stable, making it an excellent sound absorber[85–86]. Pang et al.[49] prepared an efficient acoustic absorber by integrating ultrathin graphene membranes into polymer foams, creating cellular networks that enhance sound dissipation. These graphene-based membranes exhibit strong resonances and effectively absorb sound across a wide frequency range, achieving a record noise reduction coefficient of 51.3 at a thickness of 30 mm (Fig. 10a, b). This method is scalable to commercial polymer foams, resulting in a significant ≈320% increase in the average absorption coefficient across frequencies from 200 to 6000 Hz. Furthermore, the unique physical entanglement of 3D graphene with nanofiber networks further improves sound absorption. For example, Zong et al.[87] developed flexible ceramic nanofibrous sponges (FCNSs) with hierarchically entangled graphene networks, which combine open-cell structures, closed-cell walls, and intricate fiber networks (Fig. 10c). These FCNSs demonstrate enhanced broadband noise absorption, with a noise reduction coefficient of 0.56 in the 63–6300 Hz range (Fig. 10d, e). Additionally, ultrafine fiber sponges with ultrathin graphene-based vibrators (VSFSs) were synthesized using a combination of humidity-assisted electrospinning and electrospraying[88]. Thanks to the vibration effect of the ultrathin graphene-based vibrators and the viscous friction of the porous fiber network, the VSFSs achieve effective sound absorption at both low frequencies (absorption coefficient of 0.98 at 680 Hz) and high frequencies (coefficients above 0.8 from 2000 to 6300 Hz) simultaneously (Fig. 10f-h). Notably, the lightweight VSFSs (30 mm thick) achieve a noise reduction coefficient (NRC) of 0.63, reducing high-decibel noise by up to 24.4 dB.

5 Thermal energy storage and conversion based on 3D graphene

5.1 Photothermal conversion

The utilization of solar energy has garnered significant attention in recent years, driven by the growing disparity between economic development and energy shortages. Photothermal conversion stands out for its theoretical efficiency, as it directly converts solar energy, presenting a sustainable solution to this issue[89–90]. To optimize solar energy utilization, researchers have concentrated on developing photothermal materials that exhibit broad sunlight absorption and high conversion efficiency. These materials include metals, semiconductors, carbon-based materials, and conjugated polymers. Among them, carbon-based materials, particularly 2D graphene and its derivatives, are considered ideal for photothermal applications due to their exceptional chemical stability, wide light absorption range, and lightweight nature[91]. Nevertheless, the light absorption of graphene is still

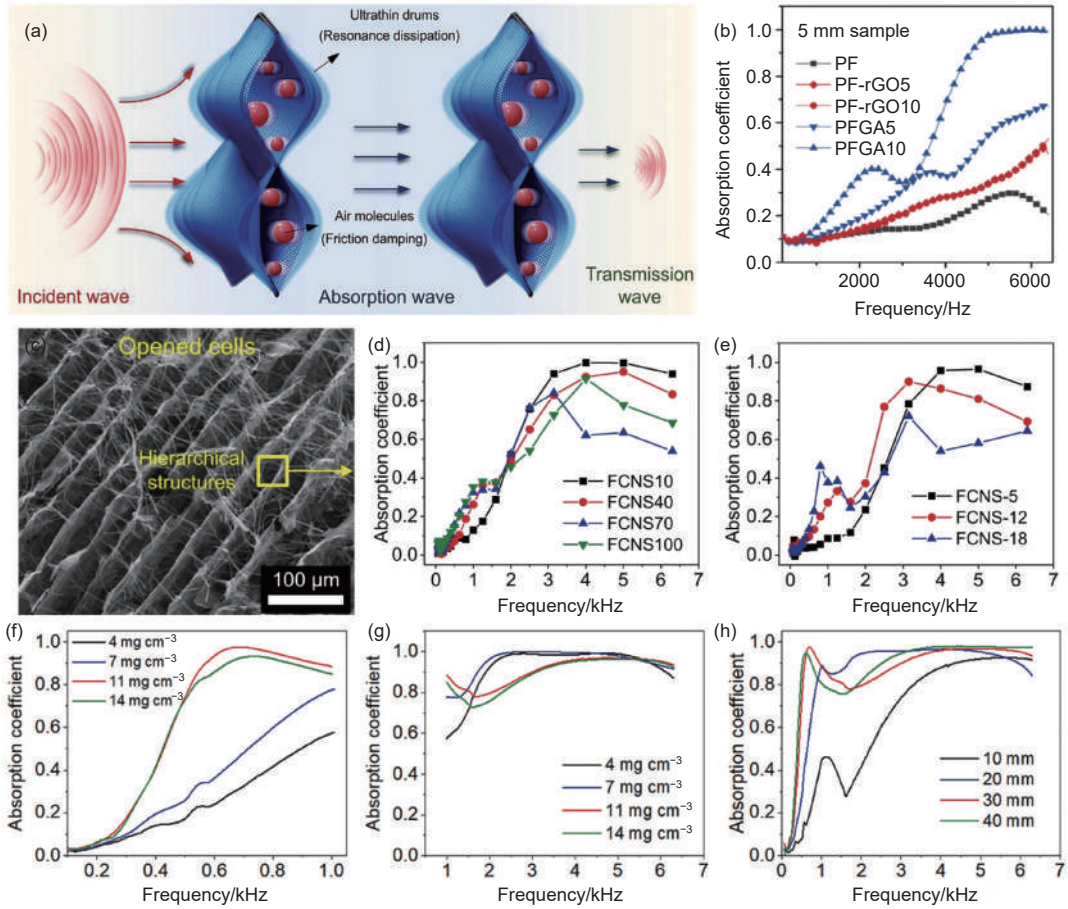

Fig. 10 (a) The mechanisms of the graphene-based absorber to achieve superior absorption by the resonance of ultrathin graphene and air friction damping in the pores. (b) The sound-absorption coefficients of PF, PF-rGO, and PFGA (Reproduced with permission, Copyright 2022, John Wiley and Sons[49]). (c) SEM image of FCNSs. (d) The absorption coefficient of the relevant FCNSs. (e) Effects of density on the absorption coefficient of FCNSs (Reproduced with permission, Copyright 2021, Springer Nature[87]). Sound absorption coefficients of VSFSs in (f) 100-1000 Hz and (g) 1000-6300 Hz. (h) Sound absorption coefficients of VSFSs with different thicknesses (Reproduced with permission, Copyright 2023, American Chemical Society[88])

constrained by its moderate reflection, which is determined by its intrinsic refractive index, as described by the Fresnel equation[92].

The multilevel structures create a refractive index gradient between the air and the coating, effectively reducing light reflection[93]. This design offers a potential approach for creating omnidirectional, low-reflectivity 3D graphene materials. Peng et al.[94] fabricated a graphene film with densely arranged porous graphene by laser scribing polybenzoxazine resin (Fig. 11a, b). This hierarchical structure significantly minimized light reflection. Thanks to the inherent photothermal conversion properties of graphene, the 3D graphene film exhibited an impressive light absorption of 99.0% across the full sunlight wavelength range. As shown in Fig. 11c, the film demonstrated excellent light-to-heat conversion performance, reaching 87.7 °C within 30 s under simulated sunlight, with an equilibrium temperature of 90.7 ± 0.4 °C. Similarly, inspired by the multilevel structures of flowers, Tian et al.[95] reported the creation of a graphene microflower (GM) material with a gradient refractive index surface. This was fabricated on polymer substrates using a UV-intense laser-induced phase explosion technique. The refractive index gradient reduces light reflection and enables the material to absorb at least 96% of light at incident angles ranging from 0° to 60° across the entire solar wavelength spectrum (200–2500 nm). Additionally, the light absorption is enhanced through multiple interferometric phase cancellations and localized surface plasmon resonance, resulting in a steady-state temperature 60 °C higher than ambient conditions under one-sun irradiation. The maximum rate of temperature rise reached

62 °C s^{-1} (Fig. 11d, e). However, achieving efficient absorption with thicknesses much smaller than the wavelength remains challenging, particularly given the common belief that ultrathin films can absorb no more than 50% of incident light. To address this, Liao et al.[96] drew inspiration from the honeycomb mirror design found in crabs' compound eyes and developed a highly light-absorbing and mechanically stable ultrathin absorber for photothermal conversion (Fig. 11f-h). With hollow apertures surrounded by a self-supporting ultrathin film of rGO and gold nanoparticles, the absorber exhibits spoof-plasmon-enhanced broadband absorption in the solar spectrum and low radiative decay in the infrared. Specifically, a strong absorption of 87% was achieved by apertures with a cross-sectional thickness of 1/20 of the wavelength, which is 7.3 times greater than that of a planar counterpart made from the same material. Additionally, the absorber demonstrates high photothermal conversion efficiency of 64%, with a hot-electron temperature reaching up to 2344 K (Fig. 11i).

5.2 Thermal energy storage and management

Phase change materials (PCMs) are a group of substances that can absorb and release significant amounts of thermal energy as they undergo a phase change. Over the past two decades, thermal energy storage systems based on PCMs have gained increasing attention, primarily due to their excellent heat storage capacity and efficient thermal energy regulation. However, a key limitation of PCMs is their low thermal conductivity, which hinders the rate of heat charging and discharging during the phase change process[97–98].

3D graphene can be used as a filler material added directly into PCMs to create phase change composites (PCCs) with enhanced thermal conductivity.

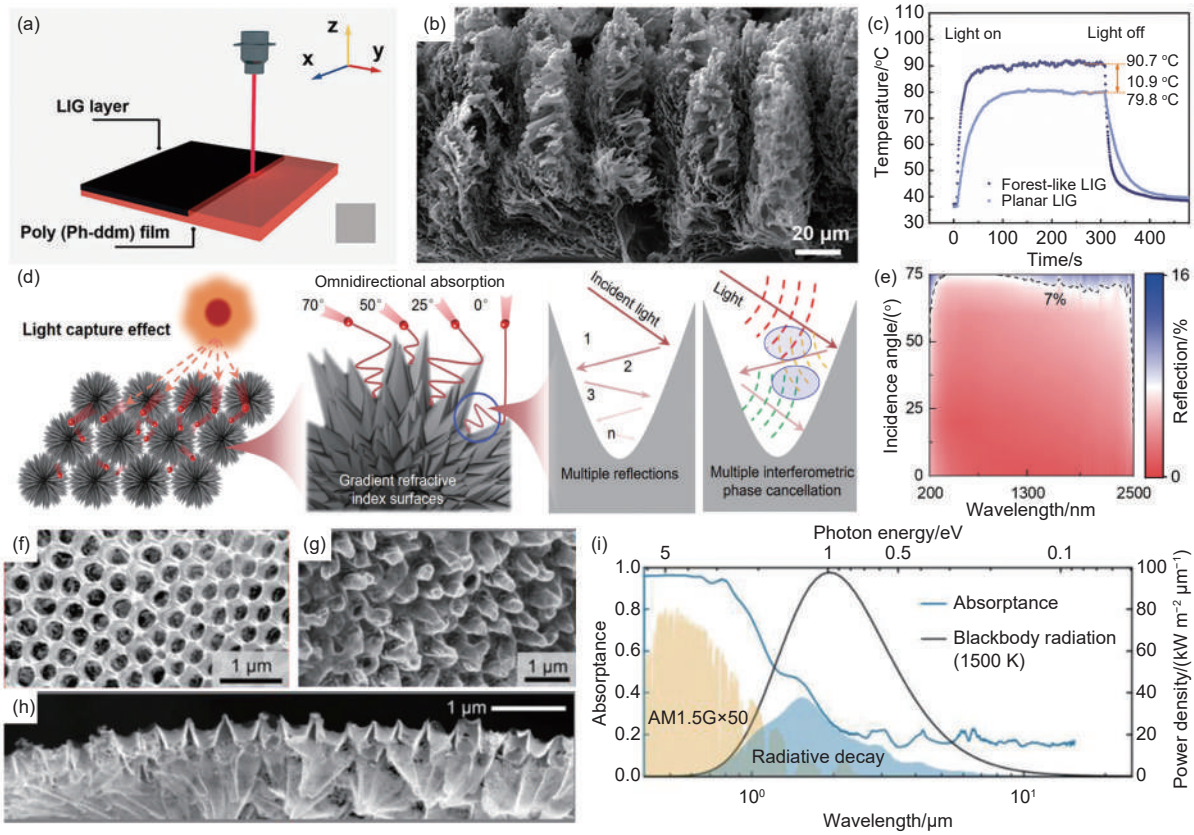

Fig. 11 (a) Schematic illustration for the preparation of forest-like LIG. (b) SEM image of forest-like LIG. (c) Temperature of dry LIGs against time under 1 sun irradiation (Reproduced with permission, Copyright 2021, American Chemical Society[94]). (d) Schematic diagram of the omnidirectional, wide-range absorption of light by the GM with a spiny surface. (e) Reflectance spectra of GM with spiky surface at different incident angles (Reproduced with permission, Copyright 2024, American Chemical Society[95]). SEM image of the (f) top surface, (g) bottom surface and (h) cross section of c-UPA. (i) Spectral absorptance (emittance) of c-UPA and its high solar absorption (for AM1.5 G) and low radiative decay (for 1500 K blackbody) (Reproduced with permission, Copyright 2024, John Wiley and Sons[96])

This addition helps achieve a more uniform temperature distribution, minimizing the formation of hotspots and preventing localized overheating. In addition to improving thermal conductivity, incorporating multifunctional 3D graphene also addresses issues such as leakage, mechanical strength, and photothermal conversion performance in PCMs[98–100]. Xi et al.[101] prepared super-hydrophilic reduced graphene oxide (RGO) aerogels, modified with konjac glucomannan (KGM), as supporting structural materials. These aerogels effectively absorb and convert visible sunlight into thermal energy. When combined with PCMs, the super-hydrophilic aerogels also help mitigate leakage problems. Under 1-sun irradiation, the sodium acetate trihydrate/KGM-modified GO aerogel (SAT/KRGO) composite PCM demonstrated a high photothermal conversion efficiency of 86.3%, owing to its excellent light absorption properties (Fig. 12a). Additionally, the number of cycles had no significant impact on the supercooling behavior of the composite material, indicating stable thermal cycling and reliable thermal storage (Fig. 12b, c). However, the chal-

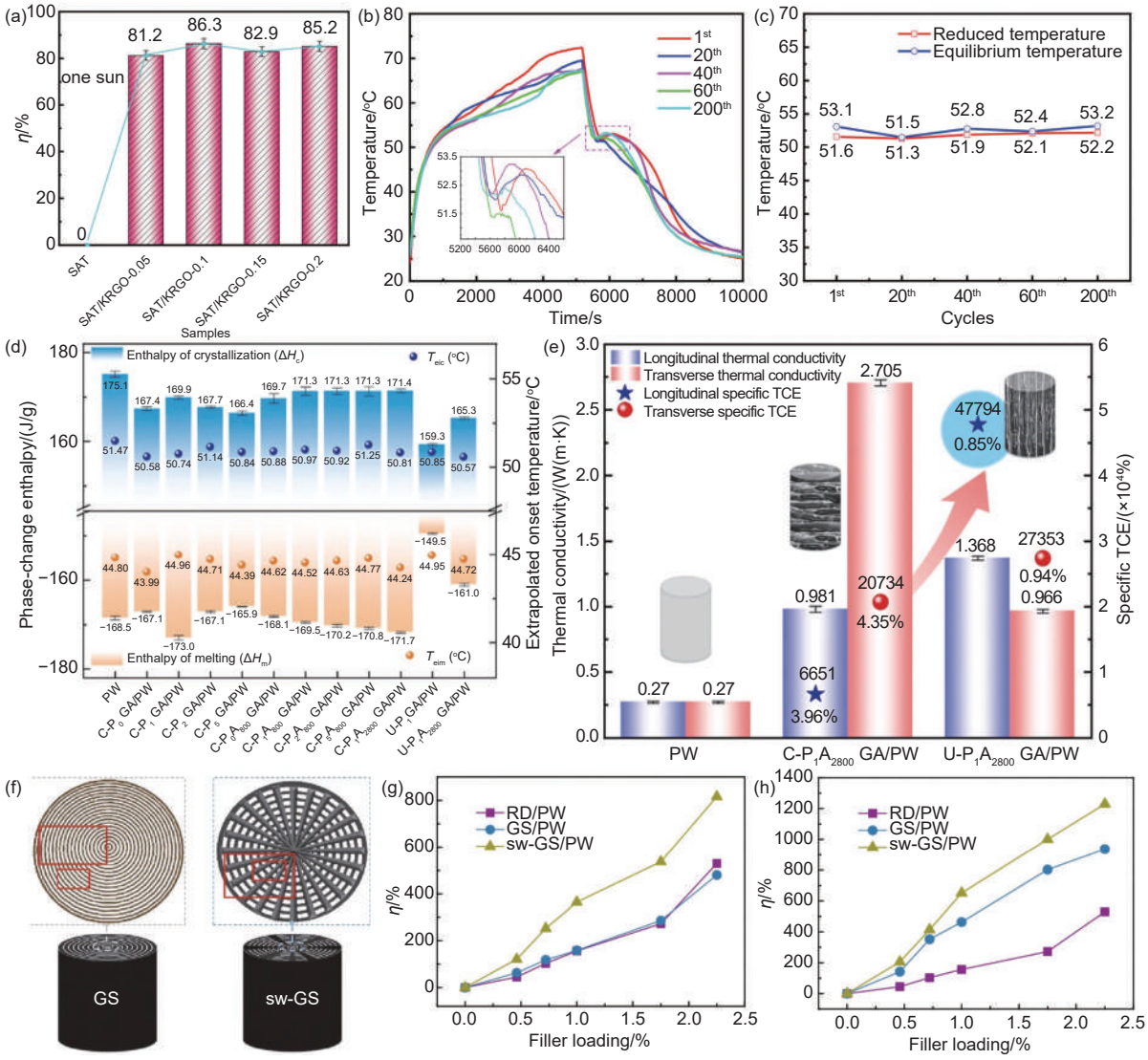

Fig. 12 (a) Photothermal conversion curves of SAT/KRGO-0.15 with different cycles under 1 sun. (b) Undercooling changes of SAT/KRGO-0.15 with different cycles. (c) Photothermal conversion efficiency of SAT and SAT/KRGO (Reproduced with permission, Copyright 2022, American Chemical Society[101]). (d) Enthalpies (ΔH_m and ΔH_c) and extrapolated onset temperatures (T_{eim} and T_{eic}) of composites. (e) Thermal conductivities of C-P1A2800 GA/PW and U-P1A2800 GA/PW in longitudinal and transverse directions and corresponding specific TCEs (Reproduced with permission, Copyright 2024, Elsevier[102]). (f) SEM images of SW-GS aerogels. Thermal conductivity enhancement in (g)longitudinal direction and (h) transverse direction of PW composites (Reproduced with permission, Copyright 2024, Springer Nature[103])

lenge of creating thermally conductive composite PCMs with low graphene aerogel content remains unresolved. To address this research gap, Liang et al.[102] synthesized poly(vinyl alcohol) (PVA)/graphene aerogels (PGAs) by hydrothermal reaction and freeze-drying methods. After annealing and paraffin wax impregnation, the resulting composite PCMs demonstrated exceptional shape stability. As shown in Fig. 12d, the composite exhibits a low density (0.82 g cm^{-3}) and a high enthalpy (165 J g^{-1}). Importantly, the integration of PVA and graphene enables the composite to achieve an ultralow graphene aerogel content (0.85%) while retaining high thermal conductivity (1.37 W m^{-1} K^{-1}), yielding a specific thermal conductivity enhancement factor of 477 (Fig. 12e). Although constructing 3D thermally conductive networks within PCMs can overcome the challenge of achieving high thermal conductivity at low filler loadings, the inherent anisotropy of such frameworks often results in poor thermal conductivity perpendicular to the filler alignment. To overcome these limitations, Lin et al.[103] drew inspiration from the hierarchical structure of spider webs and developed a phase change composite (SW-GS/PW) featuring a bioinspired 3D spider web-like graphene skeleton (Fig. 12f). Remarkably, the SW-GS/PW composite achieves simultaneous cross-plane and in-plane thermal conductivity enhancements of ~ 1260% and ~ 840%, respectively, at an ultralow filler loading with a volume of 2.25% (Fig. 12g, h).

6 Optics-related energy conversion based on 3D graphene

6.1 Photovoltaic

Solar energy, as the cleanest and most abundant energy source, is used not only for heat generation but also for electricity production. Graphene, known for its high transparency and conductivity, is widely used in solar cells as functional layers to create highly efficient photovoltaic devices[104–105]. However, 2D graphene sheets tend to form irreversible aggregates due to π-π interactions, which can reduce electron transport efficiency. In contrast, 3D graphene materials, with their unique structure and enhanced conductivity, are considered promising alternatives[106].

Dye-sensitized solar cells (DSSCs) can achieve a relatively low electron-hole recombination rate, where photoelectrons are generated by photosensitive dyes and transferred through a semiconductor under sunlight. This enables higher photovoltaic conversion efficiency. Yao et al.[107] incorporated ternary active components into the counter electrode (CE) materials to enhance the photoelectric conversion efficiency (PCE) of DSSCs. As shown in Fig. 13a, NiS nanosheets are first attached to the surface of N-doped hollow thin-shell carbon spheres (NHCS), then coated with reduced graphene oxide (RGO) to form an NHCS/NiS/RGO nanocomposite. In Fig. 13b, the large surface area of RGO promotes charge transfer through interfacial charge polarization, while the evenly distributed NiS nanosheets on NHCS surfaces capture electrons, strengthening interfacial coupling and boosting charge transfer. This also enhances triiodide oxidation and reduction, resulting in remarkable ternary functional electrode activities. As a result, the NHCS/NiS/RGO nanocomposite as a CE achieves a PCE of 9.32%, outperforming Pt-based CEs (8.06%) as shown in Fig. 13c. Additionally, quantum dot-sensitized solar cells (QDSSCs) have gained attention due to their ease of fabrication and low cost, serving as a variant of DSSCs. Zhang et al.[108] developed 3D graphene networks (GNs) and C-dot grafted graphene (CD-G) hybrids, which were incorporated into TiO_2 photoanodes to improve the performance of CdS/CdSe QDSSCs. When 1.6% of GNs and 2.0% of CD-G were added, the photoelectric conversion efficiency (η) improved from 4.04% to 4.37% and 4.69%, respectively. These improvements are mainly due to the reduced electron recombination between TiO_2 and graphene, enhancing charge carrier transport. For the CD-G/TiO_2 hybrid, electron transport from C-dots to graphene further strengthens this effect. Furthermore, the large-scale application of unassisted artificial photosynthesis (APS) devices is hindered by the need for expensive noble metal-based catalysts in photovoltaics. To address this, a well-

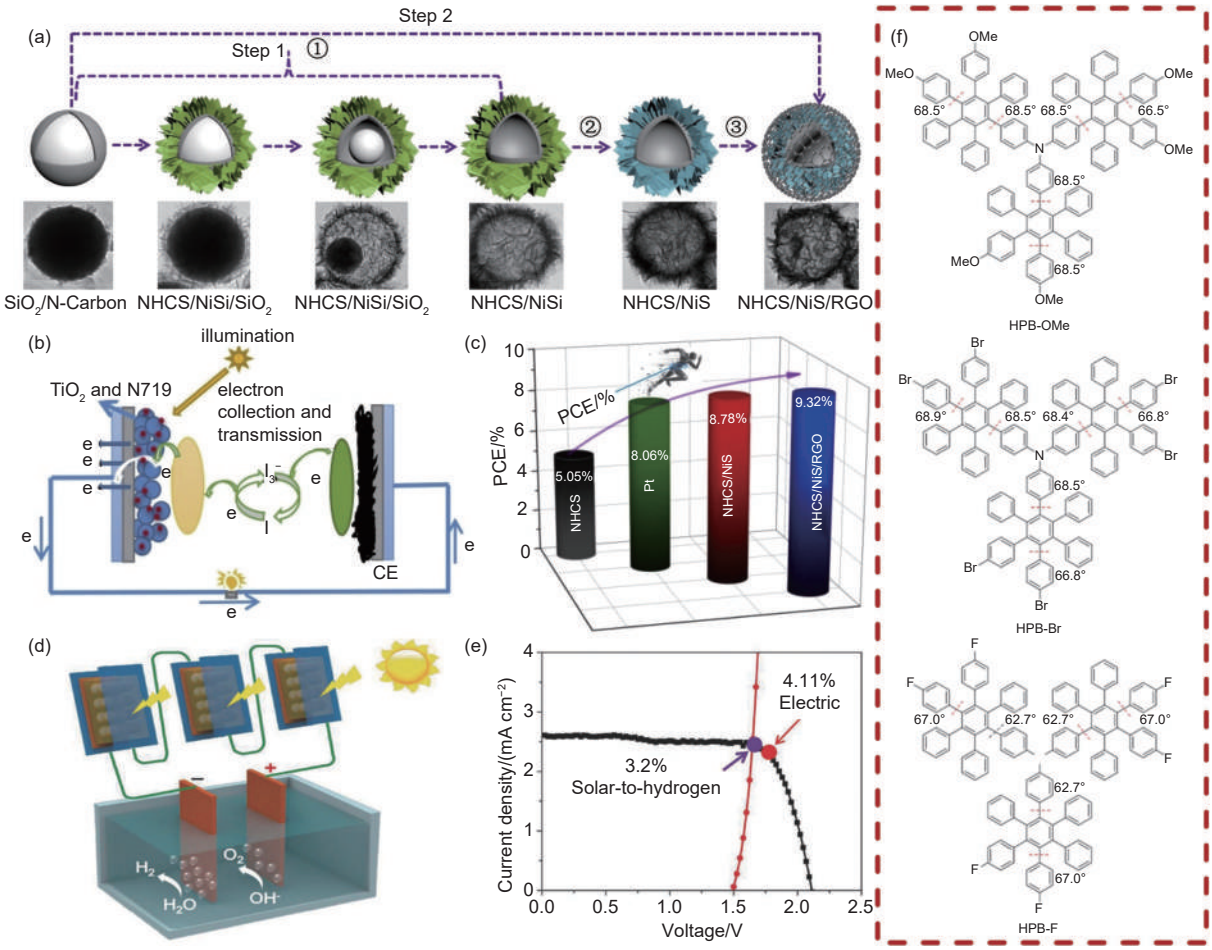

Fig. 13 (a) Two steps fabrication of the NHCS/NiS/RGO composites. The images in the top line are imagination maps, while the images in the bottom are the images recorded by TEM at different stages. (b) A conceptual diagram of structural change effects on electronic transportation. (c) The value of PCE for all samples including a DSSC with the CE made of Pt (Reproduced with permission, Copyright 2019, Elsevier[107]). (d) Schematic diagram of the unassisted APS device. (e) J-V curves of the Ni_xS_y NW/NGF-based DSSC tandem cell and the Ni_xS_y NW/NGF on nickel foam electrodes in a two-electrode system (Reproduced with permission, Copyright 2018, John Wiley and Sons[109]). (f) Ground state optimize geometries of neutral HPB molecules (Reproduced with permission, Copyright 2023, Elsevier[110])

aligned 2D Ni_xS_y nanowall (Ni_xS_y NW) structure on 3D nitrogen-doped graphene foam (NGF) was synthesized and used in unassisted APS[109]. The positive synergistic effect between the electrocatalytic activity of Ni_xS_y NW and the conductivity of NGF makes the (2D/3D) Ni_xS_y NW/NGF composite highly efficient as a counter electrode for DSSCs. As shown in Fig. 13d, three Ni_xS_y NW/NGF-based DSSCs are connected as a tandem cell for unassisted solar-driven water splitting. Impressively, this integrated photovoltaic-electrolyzer APS device achieves a solar-to-hydrogen conversion efficiency of 3.2% with excellent stability (Fig. 13e).

3D graphene materials also show great potential for improving the efficiency and stability of perovskite solar cells (PSCs). For instance, Hanmandlu et al.[110] used 3D nanographene (NG) precursors with well-defined molecular structures and various functional groups (F, Br and OMe) to achieve efficient inverted PSCs (Fig. 13f). The 3D NG precursor created a bridge between the perovskite film and the hole transport layer, reducing interfacial defects. It also passivated defect states within the bulk perovskite through an automatic bottom-up passivation process. Both computational simulations and experimental data showed that the functional groups of the 3D NG precursors bonded strongly with the perovskites, forming F-Pb, Br-Pb and OMe-Pb coordination bonds. These synergistic effects resulted in significant improvements in the photovoltaic performance of the inverted

PSCs, with an absolute efficiency increase of over 3%.

6.2 Photocatalysis

In photocatalytic reactions, the redox processes occur primarily on the surface of the photocatalyst, rather than in the surrounding liquid medium. Effective photocatalysis relies not only on efficient charge separation and transfer but also on the ability of the photocatalyst's surface to adsorb reactants at its active sites[37]. Therefore, designing photocatalysts with a high density of active sites is essential for enhancing both the yield and selectivity of the desired products[111]. 3D graphene has gained attention as a photocatalyst due to its unique structure and properties, including a hierarchical network, large specific surface area, diverse pore distribution, strong light absorption, and excellent electrical conductivity. The large surface area and porous structure of 3D graphene help maximize the exposure of active sites, while also promoting electron transfer and the diffusion of gas products.

Converting solar energy into fuels and chemicals through photochemical methods offers great potential for meeting global energy needs. For example, Tam et al.[112] designed a graphene hydrogel composite for hydrogen evolution through photocatalytic seawater splitting (Fig. 14a). As shown in Fig. 14c-e, they created phosphorus-doped graphene quantum dots (PGQDs) with different phosphorus bonding configurations (PC_3, PO_4 and PO_3), which were then combined with graphene hydrogel to form the $PGQD_3$/GH composite. The $PGQD_3$/GH composite, with PC_3 bonds, exhibited a tunable electronic structure and significantly enhanced visible light absorption (Fig. 14b). As a result, the $PGQD_3$/GH composite showed excellent photocatalytic hydrogen production, achieving a yield of 20.47 mmol g^{-1} h^{-1} in seawater splitting (Fig. 14f). Additionally, Maouche et al.[113] developed a 3D N-doped graphene aerogel (3DNG) by combining graphitic carbon nitride with GO. The 3DNG, with a large surface area of 536 m^2 g^{-1} and a band gap of 2.42 eV, demonstrated high hydrogen production under visible light. Characterization revealed that the porous 3D structure, hydrogen bonding, π-π interactions, and improved charge transfer due to nitrogen doping were key factors enhancing the photocatalytic performance of this 3DNG catalyst.

The growing environmental pollution caused by industrial chemicals calls for the development of simple methods for their removal. Among the various techniques, photocatalytic degradation is particularly appealing because it requires no additional chemicals, relying solely on light and atmospheric oxygen to break down pollutants. Additionally, 3D graphene-based photocatalysts have been widely studied for pollutant removal due to their unique benefits. For instance, Chen et al.[114] developed a composite by encapsulating AgBr inside rGO, which could be integrated into graphene to form hydrogels with 3D network structures. The core-shell structure prevented excessive growth of AgBr particles, ensuring their size remained controlled (500–600 nm). The hybridization with graphene also facilitated the rapid migration and separation of photogenerated charges. Bisphenol A (BPA) was efficiently adsorbed by the 3D graphene nanosheets and quickly degraded by nanoparticles under visible light, demonstrating that the combination of adsorption and photocatalytic degradation greatly improved pollutant removal efficiency. The results showed a 1.5-fold increase in BPA removal compared to pure AgBr, with removal rates above 90% after 5 cycles. BPA degradation remained at 100% for the first 6 h under continuous flow conditions. In another study, Yan et al.[115] reported a rGO/polypyrrole hybrid aerogel with highly efficient photodegradation and ultra-high solar-powered water evaporation for freshwater production and wastewater decontamination (Fig. 14g). In this 3D hybrid aerogel, the π-π interactions between the 2 components not only prevented the stacking of rGO nanosheets, creating ample water transport channels and ensuring mechanical stability (Fig. 14h-j), but also enhanced interactions with organic molecules, resulting in high removal efficiency for volatile organic compounds (VOCs). Consequently, the wide-spectrum light absorption, photothermal effects, and solar-driven photocatalysis in the hybrid aerogel significantly boosted

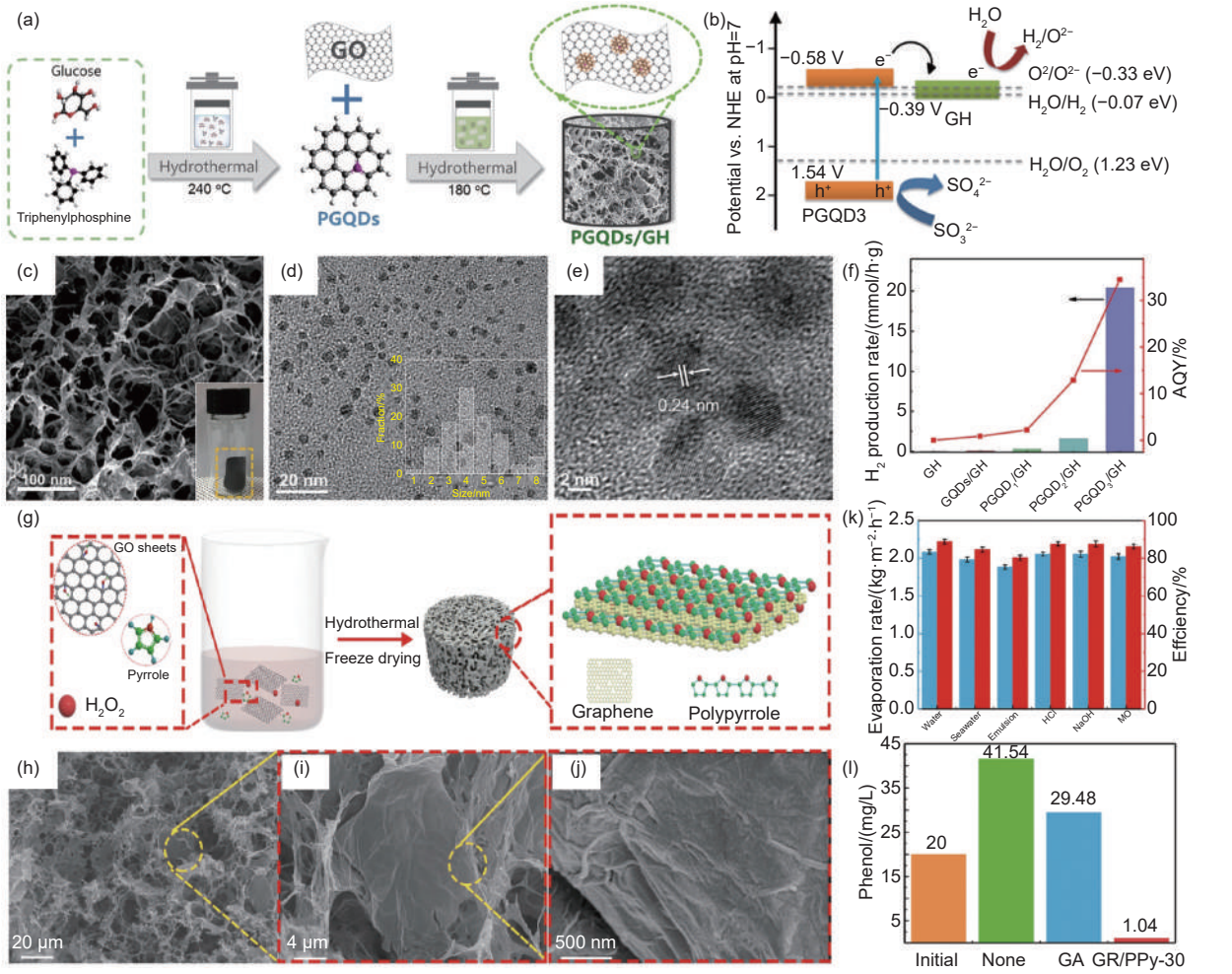

Fig. 14 (a) Schematic illustration for the preparation of PGQDs and PGQDs/GH composites. (b) The schematic illustration of the band energy diagram for photoinduced charge transport and photocatalytic mechanism for H_2 evolution at $PGQD_3$ and GH interface. (c) SEM, (d) TEM and (e) HREM images of $PGQD_3$. (f) The photocatalytic H_2 production rate and AQY in seawater using the prepared PGQDs/GH composites (Reproduced with permission, Copyright 2024, Elsevier[112]). (g) Schematic illustration of the synthetic process of GR/PPy aerogels. (h-j) SEM images of the GR/PPy aerogel under different magnification. (k) Corresponding evaporation rate and energy conversion efficiency of GR/PPy-30 in different water sources under 1.0 sun irradiation. (l) Corresponding concentration of phenol on different evaporators (Reproduced with permission, Copyright 2022, Elsevier[115])

the thermal-assisted photodegradation of VOC-contaminated water, achieving a water evaporation rate of 2.08 kg m^{-2} h^{-1} and a phenol removal efficiency of 94.8% (Fig. 14k, l).

6.3 Laser-produced X-ray sources

Plasma physics, when integrated with materials science, nuclear science, radiation detection, and advanced laser technology, opens up new research opportunities of both fundamental and practical importance[116]. In this context, laser-plasma-based ion acceleration offers a promising alternative to traditional accelerators, overcoming several key limitations, such as fixed energy levels, radiation protection concerns, high costs and large, non-portable sizes[117].

In this regard, Cao et al.[118] used 2D particle-in-cell simulations to demonstrate that a target with sub-wavelength nanolayered surfaces can reduce reflection and increase energy absorption from intense short laser pulses. The conversion of laser energy to electron energy can be improved by optimizing the vacuum gap between the nanolayers, as this changes the phase structure of the laser field in the target. Additionally, 3D graphene, assembled from atomically thin 2D graphene sheets, forms highly porous, low-density multi-level structures. This design could offer a potential solution for enhancing the intensity of X-ray pulses generated by laser-produced plasma.

Li et al.[119] proposed a method to improve the ab-

sorption efficiency of ultra-intense femtosecond lasers by using carbon aerogel targets. Compared to a uniform target with the same density, the carbon aerogel target significantly increases laser absorption, achieving a maximum efficiency of 88%. This high absorption efficiency is due to the porous structure and larger surface area of carbon aerogel, which allows the laser to penetrate deeper into the target and interact more effectively with the particles, rather than being reflected off the surface. In another study, a 3D multi-walled carbon nanotube array target was used to increase the efficiency of water-window and *K*α X-ray pulse conversion from femtosecond-laser-produced plasma[120]. The X-ray fluence in the water-window region increased sevenfold compared to a conventional carbon plate target, and the soft X-ray pulse duration was 26 ps. Additionally, the *K*α X-ray emission from a Si substrate covered with a carbon nanotube array was also enhanced. This suggests that covering different solid materials with 3D carbon nanotube arrays could generate stronger short *K*α X-ray pulses at the corresponding wavelengths. Furthermore, Ji et al.[121] used 2D particle-in-cell simulations to investigate the propagation of laser-driven energetic electrons in a 3D carbon nanotube array target. The results showed that laser energy is more effectively transferred to electrons in the nanotube array than in a flat foil, due to the hole structures in the array. Energetic electrons are efficiently generated when the array is irradiated by a short, intense laser pulse, and their movement is confined and guided by the strong transient electromagnetic fields generated at the walls of the nanotubes.

7 Electromagnetic energy absorption and electrostatic energy storage based on 3D graphene

7.1 Electromagnetic shielding and wave absorption

With the rapid advancement of information technology, high-power electronic devices are increasingly integrated into various aspects of daily life. However, this widespread adoption has led to growing concerns about issues such as electromagnetic interference, radiation pollution and information leakage. These challenges have become significant topics of interest in contemporary society[122–123]. As a result, the development of electromagnetic absorbing materials has emerged as a key area of research. Effective electromagnetic absorbers typically feature low dielectric constants, moderate complex permittivity, and balanced electrical conductivity. Some of the well-known developed absorbers include ferrite magnetic metals and their oxides, dielectric loss materials such as carbon-based nanostructures, conductive polymers, and ceramics. However, these materials have limitations, including poor impedance matching, narrow effective absorption bandwidth, low thermal and corrosion resistance, and high filler content, which restrict their practical use[124]. Furthermore, the focus of research has shifted towards materials that are lightweight, flexible, broadband, and possess low weight, all of which are essential for improving their practical applications[40].

3D graphene offers a unique combination of high porosity, low density, large specific surface area, and high compressibility. Its internal porous structure and 3D network effectively address the issues of graphene sheet agglomeration, high conductivity, and impedance mismatch typically observed in 2D graphene, thereby enhancing its microwave absorption performance. Huang et al.[125] synthesized graphene foam by a CVD method, where the walls of the foam were composed of two to five graphene layers. These layers were interconnected to form a low-density, porous network with a broad distribution of pore sizes and high electrical conductivity (Fig. 15a, b). The distinctive structure of this graphene foam results in exceptional electromagnetic shielding, with its electromagnetic interference shielding effectiveness (>720 dB cm^3 g^{-1}) and absolute shielding effectiveness (>45 000 dB cm^2 g^{-1}) surpassing that of most other materials (Fig. 15c). In addition, Xu et al.[126] reported the fabrication of honeycomb porous graphene (HPG) using laser scribing technology for electromagnetic interference shielding and wearable applications.

Due to its honeycomb structure, HPG achieved an electromagnetic interference shielding effectiveness of up to 45 dB at a thickness of 48.3 μm. The single-piece HPG also demonstrated an ultrahigh absolute shielding effectiveness of 240 123 dB cm^2 g^{-1}, coupled with an extremely low density of 0.0388 g cm^{-3}.

Furthermore, 3D graphene has been widely explored in conjunction with various materials, including carbon-based compounds, conductive polymers, and magnetic materials, to improve microwave absorption performance. For instance, Huang et al.[127] presented the microwave absorption characteristics of MOF/rGO-derived magnetic and dielectric aerogels, such as Ni-doped Fe_3O_4@C/rGO (Fig. 15d-g), which exhibited exceptional electromagnetic absorption properties. As shown in Fig. 15h and i, these materials displayed strong absorption and broad bandwidth at low thicknesses of 2.5 mm (−58.1 dB, 6.48 GHz) and 2.8 mm (−46.2 dB, 7.92 GHz). Furthermore, MXene and Ag nanowires (Ag NWs) have been employed to cover the honeycomb structure of HPG, enhancing surface reflection. This modification allows the HPG/Ag NWs composite membrane to achieve an impressive absolute shielding effectiveness of 292 754 dB cm^2 g^{-1}. Besides, Ghaffarkhah et al.[128] developed ultra-lightweight cryogels composed of $Ti_3C_2T_x$/GO by controllable templating using filamentous-structured liquids, avoiding the need for chemical or thermal reduction. These cryogels, with densities ranging from 3 to 7 mg cm^{-3}, demonstrate exceptional electromagnetic interference shielding effectiveness, ranging from 33 000 to 50 000 dB cm^2 g^{-1}. Additionally, when $Ti_3C_2T_x$/GO cryogels are used as the

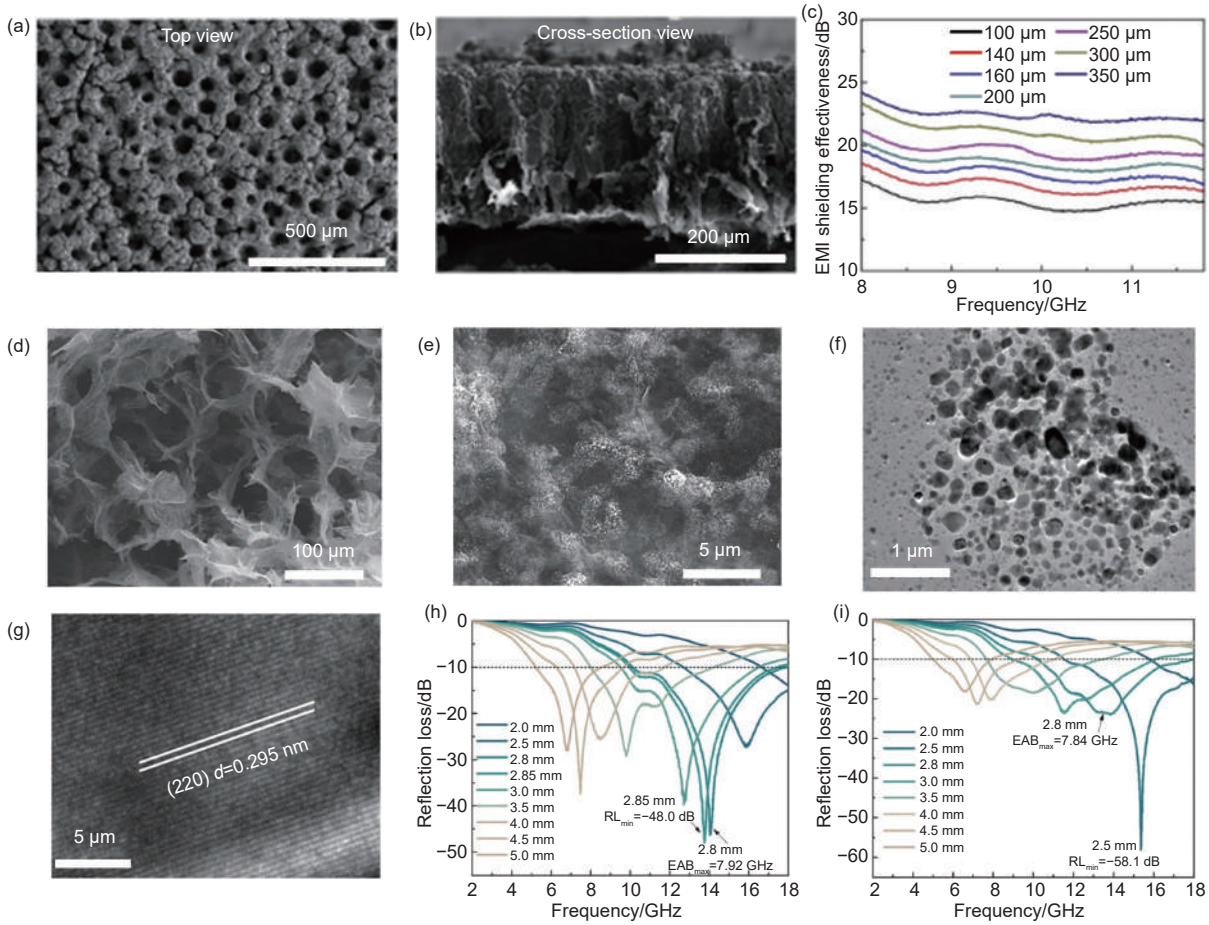

Fig. 15 SEM images of the (a) top surface and (b) cross-sectional of the graphene foam. (c) Electromagnetic interference shielding effectiveness of sheets of the graphene foam with different thicknesses in the frequency range 8-12 GHz (Reproduced with permission, Copyright 2020, Elsevier[125]). (d, e) SEM and (f, g) TEM images of the Ni-doped Fe_3O_4@C/rGO aerogel. (h, i) RL-*f* curves of Ni-doped Fe_3O_4@C/rGO aerogel (Reproduced with permission, Copyright 2020, Springer Nature[127])

foundation for conductive epoxy nanocomposites, electromagnetic interference shielding effectiveness improves to 31.7–51.4 dB, even with a low filler loading (0.3%–0.7%).

7.2 Supercapacitors for electrostatic potential energy storage

The performance of supercapacitor electrodes depends on three key factors: electrical conductivity, electrolyte ion transport efficiency, and active material properties[129]. Recent advances in 3D graphene materials have enabled high-performance supercapacitor electrodes due to their large specific surface area (SSA), excellent conductivity, and tunable porous structures. For example, Qin et al.[130] developed hierarchical nanoporous graphene (hnp-G) films with pore sizes ranging from 1 to 150 nm for electrode applications. These films were synthesized by coating nanoporous copper with hydrogenated graphite by low-temperature CVD, followed by high-temperature catalytic pyrolysis. The hnp-G exhibits an ultrahigh SSA of 1160 m^2 g^{-1}, ensuring unobstructed ion transport channels. Critically, the 3D hierarchical porosity and strong wettability of hnp-G with gel electrolytes not only prevent graphene restacking under mechanical stress but also establish continuous, short pathways for electron/ion diffusion. Consequently, flexible symmetric supercapacitors based on compressed hnp-G and gel electrolytes achieve exceptional energy density (2.65 mWh cm^{-3}), power density (20.8 W cm^{-3}), bending stability, and cycling durability (94% capacitance retention after 10 000 cycles). In a complementary approach, Li et al.[131] engineered freestanding graphene laminate film electrodes with precisely adjustable interlayer spacing for optimized pore utilization (Fig. 16a). By systematically tailoring pore sizes to match electrolyte ion dimensions, this design maximizes volumetric capacitance (Fig. 16b, c). At optimal mass loading, the resulting symmetric supercapacitor delivers a stack volumetric energy density of 88.1 Wh L^{-1} (Fig. 16e, f). Furthermore, the optimized electrode was integrated into an all-solid-state, flexible ionogel-based device capable of multi-output configurations and long-term stability.

Beyond serving directly as electrodes, 3D graphene can be integrated with high-capacitance active materials to construct hybrid supercapacitor architectures. These materials, though offering substantial charge storage, often suffer from low conductivity and cycling instability. Incorporating 3D graphene addresses these limitations by enhancing charge transfer kinetics and creating efficient ion diffusion pathways. For instance, Li et al.[132] developed covalent organic framework/reduced graphene oxide (COF/rGO) aerogels by hydrothermal assembly. The COFs grow in situ on 2D graphene sheets, which self-assemble into a 3D architecture, forming a compressible, hierarchical porous aerogel after freeze-drying. When tested as supercapacitor electrodes, these aerogels achieve a specific capacitance of 269 F g^{-1} at 0.5 A g^{-1} and retain 91% capacitance over 5 000 cycles (Fig. 16g-i). In a parallel study, Wang et al.[133] demonstrated a room-temperature, one-step scalable method to fabricate 3D macroporous graphene foams (POM-GFs). Polyoxometalates (POMs) act as crosslinkers and nucleation sites during GO reduction by hydrazine hydrate, yielding freestanding electrodes with uniformly dispersed POM nanoclusters. The POM-GFs exhibit a layered structure, high electrical conductivity (622 S m^{-1}), and exceptional capacitance: 205 F g^{-1} gravimetrically and 334 F cm^{-3} volumetrically at 1 mV s^{-1}, with 83% retention after 10 000 cycles. Solid-state devices based on POM-GFs deliver 157 F g^{-1} and 115 F cm^{-3} at 2 mV s^{-1}, alongside a volumetric energy density of 2.6 mWh cm^{-3}.

8 Electric battery based on 3D graphene

3D graphene combines all ideal characteristics necessary for electrodes of high-performance rechargeable batteries, including large specific surface area, high electrical conductivity, tunable chemistry, and mechanical rigidity. Its intrinsic conductivity and structural stability make it a compelling self-supporting electrode material. This material offers 3 critical advantages: (1) A high electrochemically active surface area; (2) Rapid charge/mass transport pathways;

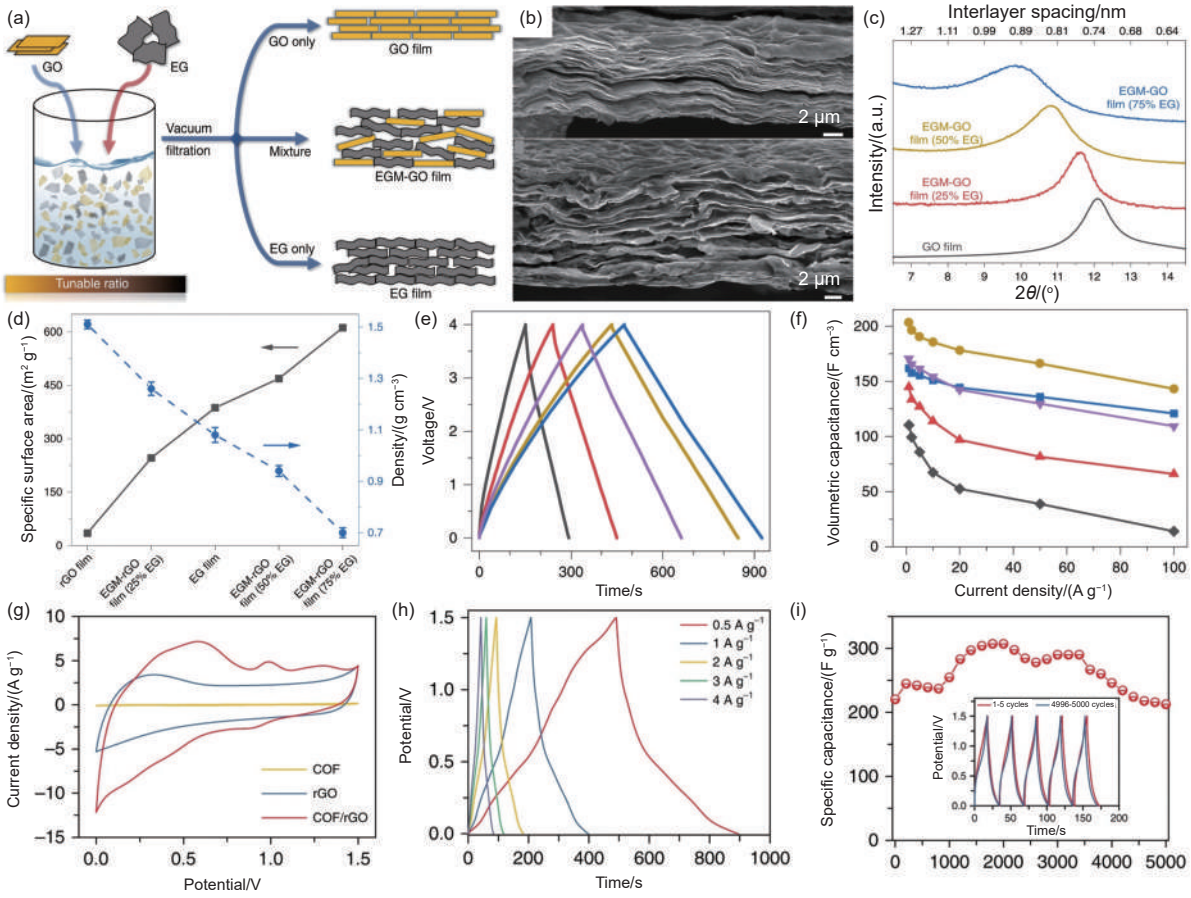

Fig. 16 (a) Schematic diagram of the production of EGM-GO films. (b) SEM images of EGM-GO films. (c) X-ray diffraction patterns and the corresponding *d*-spacing of EGM-GO films. (d) The specific surface area and bulk density of the EGM-GO films. (e) GCD curves at a current density of 1 A g^{-1}. (f) Volumetric capacitances versus current densities (Reproduced with permission, Copyright 2020, Springer Nature[131]). (g) CV curves for rGO, COF/rGO and COF at 50 mV s^{-1}. (h) GCD curves of COF/rGO at a current density of 0.5, 1, 2, 3 and 4 A g^{-1}. (i) The cyclic stability of COF/rGO at a current density of 8 A g^{-1} (Reproduced with permission, Copyright 2020, Springer Nature[132])

and (3) exceptional mechanical robustness and chemical stability. These attributes collectively enable superior battery performance. Furthermore, the lightweight nature and extreme porosity of 3D graphene frameworks make them exceptional host matrices for active materials. They not only enhance electrical connectivity but also mitigate volume expansion-induced stress during cycling through their resilient 3D architecture.

8.1 Li/Na/K ion batteries

Enhancing energy density remains critical for advancing metal-ion batteries, with high-performance electrodes being a key pathway[134–135]. Therefore, alternative carbon-based anode materials, such as hard carbon and soft carbon, have gained significant attention due to their potential for high capacity, cost-effectiveness, and low voltage. Hard carbon, with its disordered structure, enables the insertion and extraction of alkali metal ions, offering a high capacity and a low voltage plateau around 0.1 V[136]. However, its rate capability and cycling stability are limited by its relatively low electrical conductivity. Soft carbon, with its graphitic structure, provides interlayer spaces for alkali metal ion insertion and extraction[137]. Despite this, its performance in storing alkali metal ions is often suboptimal due to its limited surface area, which cannot accommodate enough active sites. In addition to carbon-based anodes, other anode materials, including metal oxides, metal sulfides, metal carbides, conducting polymers and alloys, have also been extensively investigated for alkali metal-ion batteries[138]. Most of these materials are p-type semiconductors with low electrical conductivity, making them unsuitable for high-rate applications that demand fast elec-

tron transfer. Thus, combining these materials with conductive matrices is crucial for developing high-performance anodes. In view of this situation, 3D graphene as conductive, large-surface frameworks come in handy. This improvement stems from three synergistic effects: (1) reinforced electrical pathways, (2) accelerated ion diffusion kinetics, and (3) effective mitigation of electrode volume fluctuations. For example, Wang et al.[139] demonstrated this strategy by anchoring honeycomb-like MoS_2 nanostructures on 3D graphene foam (HC-MoS_2@GF) through a surfactant-assisted solution process. The GF substrate provides dual functionality—a lightweight scaffold (1000 S m^{-1} conductivity) for rapid charge transport and a structural template guiding ordered MoS_2 growth. This hierarchical architecture delivers enhanced Li-ion storage due to its combined high surface area (312 m^2 g^{-1}), interconnected porosity, and conductive network. A complementary approach integrated ultrafine TiO_2 nanocrystals with binder-free microporous graphene (PG)[140]. Fig. 17a shows that the PG framework simultaneously enables fast electron transport through its conductive network and rapid ion access by open mesoporous channels. This dual-transport optimization achieves exceptional cyclability, maintaining 100% capacity retention over 10 000 cycles with near-perfect coulombic efficiency (Fig. 17b).

The scarcity of lithium reserves (20 mg/L in Earth's crust) and associated high costs limit lithium-ion batteries (LIBs) for grid-scale storage[141–142]. This drives research toward cost-effective alternatives like

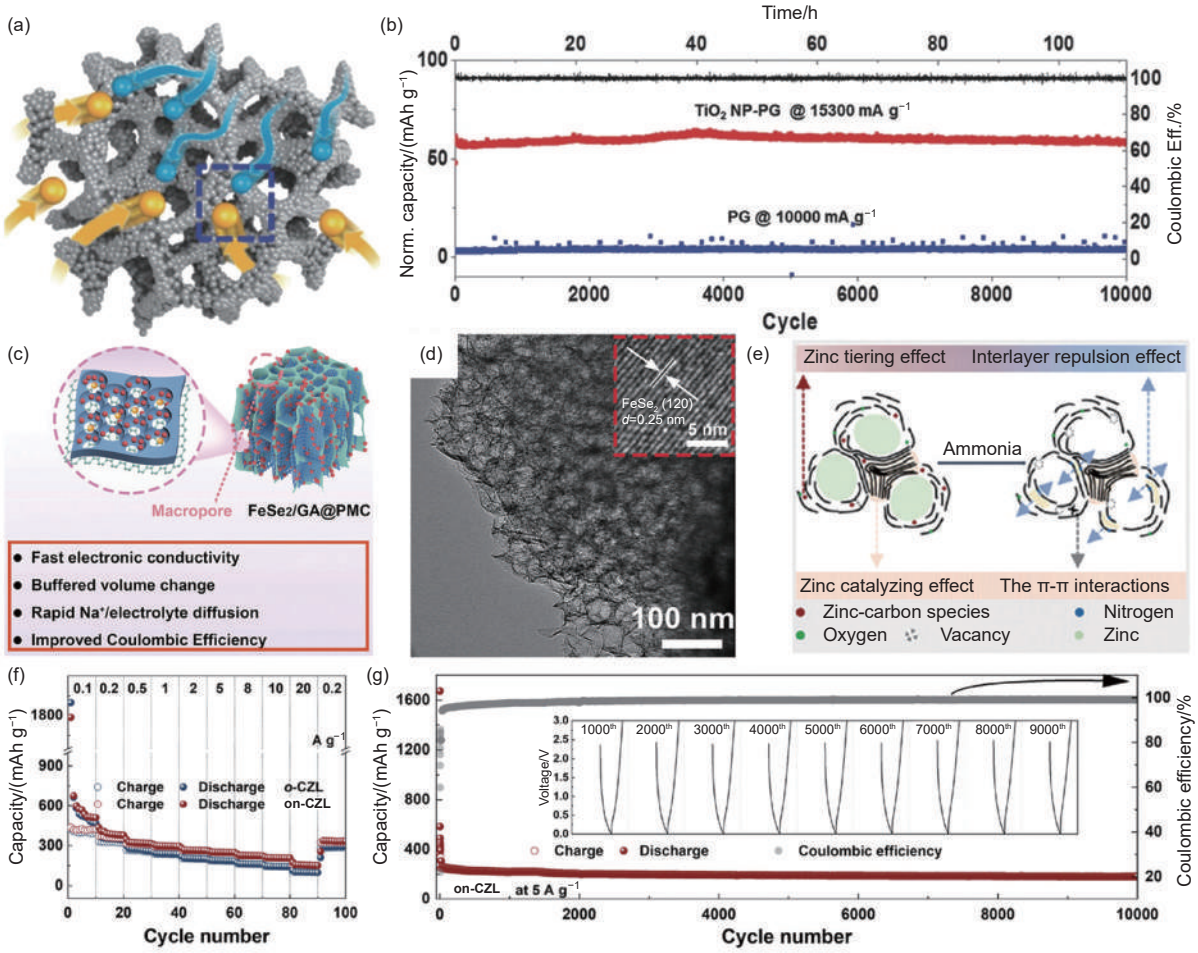

Fig. 17 (a) Schematics of proposed structures and charge carrier diffusion of the TiO_2 NP-PG. (b) Cycle life of TiO_2 NP-PG and PG (Reproduced with permission, Copyright 2016, John Wiley and Sons[140]). (c) Schematic illustration for $FeSe_2$/GA@PMC. (d) SEM images of $FeSe_2$/GA@PMC (Reproduced with permission, Copyright 2024, John Wiley and Sons[144]). (e) Sketched growth mechanism of zinc-assisted pyrolysis of lignin for growing carbon with large interlayer spacing. (f) Rate capability and (g) cycle life at 5 A g^{-1} of on-CZL anode (Reproduced with permission, Copyright 2024, John Wiley and Sons[146])

other alkali metal (Na^+, K^+) ion batteries. 3D graphene has great application prospects in these fields as well. As a typical example, Zhao et al.[143] exemplifed this by synthesizing O/N-co-doped holey graphene aerogels by employing a low-temperature selective oxidation strategy for sodium-ion battery (SIB) anodes. Controlled combustion of graphene/low-crystallinity carbon mixtures at 450 °C created elastic monoliths with in-plane nanopores and optimized crystallinity. These structural features enabled dual enhancements: (1) accelerating Na^+/electron transport through interconnected pathways and (2) increasing storage sites by heteroatom-induced interlayer expansion and surface reactivity. The optimized anode delivered 446 mAh g^{-1} at 0.1 A g^{-1}, 189 mAh g^{-1} at 10 A g^{-1}, and 81.0% capacity retention after 2000 cycles (5 A g^{-1}). Besides, a variety of active materials have been integrated into 3D nanoporous graphene to build composite electrodes. As shown in Fig. 17c and d, Tian et al.[144] designed an $FeSe_2$/GA@PMC electrode using phosphorus-doped graphene aerogel/mesoporous carbon (GA@PMC) to host $FeSe_2$ nanoparticles. In such GA@PMC, the conformal GA could improve the entire conductivity while decreasing the specific surface area directly in contact with the electrolyte. The interconnected macroporous structure not only promotes the diffusion of Na^+ but also buffers the volume change of the guest active nanoparticles. This dual-function architecture achieves exceptional rate capability and cycling stability in SIBs.

3D graphene-based materials are promising anode materials for potassium-ion batteries (PIBs) due to their high electrical conductivity[145]. For instance, Zhang et al.[49] developed a sulfur-assisted method that transforms the benzene rings of tetraphenyltin into high-purity crystalline graphene, resulting in the formation of 3D, few-layer graphene microspheres (FLGMs). When applied as an anode material in PIBs, FLGMs demonstrated a low discharge voltage, with an average discharge platform of approximately 0.1 V. Additionally, they exhibited a high initial capacity of 285 mAh g^{-1} at 50 mA g^{-1}, exceptional cycling stability (with no capacity loss after 1000 cycles at 200 mA g^{-1}), and excellent rate performance. However, many carbon-based anodes suffer from limited cycle life and poor rate capability, primarily due to the insufficient interlayer spacing of sp^2-hybridized carbon, which is incompatible with the larger ionic radius of potassium. To solve this problem, our group created a 3D macroporous graphene derived from biomass featuring an expanded interlayer spacing of 0.44 nm, achieved through zinc-assisted pyrolysis (Fig. 17e)[146]. This increased interlayer spacing facilitates faster potassium ion diffusion and mitigates the volume expansion during the potassiation process. Furthermore, the interconnected network structure shortens the transport distances for both electrons and ions. As shown in Fig. 17f and g, this material exhibited a reversible capacity of 303 mAh g^{-1} at 1 A g^{-1}, 157 mAh g^{-1} at 20 A g^{-1}, and maintained a capacity of 184 mAh g^{-1} at 5 A g^{-1} after 10 000 cycles. Additionally, Yang et al.[147] also reported the development of a 3D porous carbon framework (CFM-SNG) constructed from sulfur/nitrogen co-doped graphene nanosheets, which also exhibit an ultralarge interlayer spacing of 0.448 nm and abundant edge defects. As an anode material for PIBs, CFM-SNG demonstrated enhanced reversible capacity (348.2 mAh g^{-1} at 50 mA g^{-1}), superior cycling stability (188.8 mAh g^{-1} at 1000 mA g^{-1} after 2000 cycles), and excellent rate performance (204.3 mAh g^{-1} at 2000 mA g^{-1}).

8.2 Lithium-sulfur (Li-S) batteries

Li-S batteries are considered one of the most promising next-generation electrochemical energy storage systems due to their high theoretical specific capacity of 1675 mAh g^{-1} and energy density of 2600 Wh kg^{-1}[148]. However, several significant challenges with the sulfur cathodes have limited the practical use of Li-S batteries. These include: (1) The low electrical conductivity of sulfur and its discharge product, Li_2S; (2) Rapid capacity fading caused by the migration of soluble intermediate polysulfides to the anode; and (3) the large volumetric expansion (≈80%) from sulfur to Li_2S during lithiation. One potential solution to these issues is the use of 3D graphene with a structured framework and high electrical conductiv-

ity to load and stabilize sulfur[149–150]. As reported by Zhou et al.[23], they developed a strut-like graphene (SG) foam featuring interconnected networks, a porous structure, and stable defects, which served as an effective sulfur host for Li-S batteries (Fig. 18a-e). This SG foam enhanced the conductivity of the cathode, mitigated volume changes, facilitated electron and ion transport, and reduced the polysulfide shuttle effect. As shown in Fig. 18f-h, the sulfur-loaded SG cathode delivered excellent performance, achieving a capacity of 1442 mAh g^{-1} at 0.2 C, a high-rate capacity of 857 mAh g^{-1} at 4 C, and a cyclability of 691 mAh g^{-1} after 500 cycles at 2 C.

To improve sulfur redox kinetics, researchers have incorporated catalytic materials into 3D graphene frameworks to design high-efficiency composite cathodes. For example, Wang et al.[151] developed a sulfur host using anatase TiO_2(001) nanoplatelets anchored on porous graphene aerogel (TiO_2@GA). The TiO_2(001)/graphene lattice alignment enhanced the interfacial electron transfer compared to conventional TiO_2(101) systems. This architecture combines physical sulfur confinement through mesopores and chemical polysulfide anchoring by TiO_2-graphene bonding, yielding a S@TiO_2@GA cathode with exceptional discharge capacity

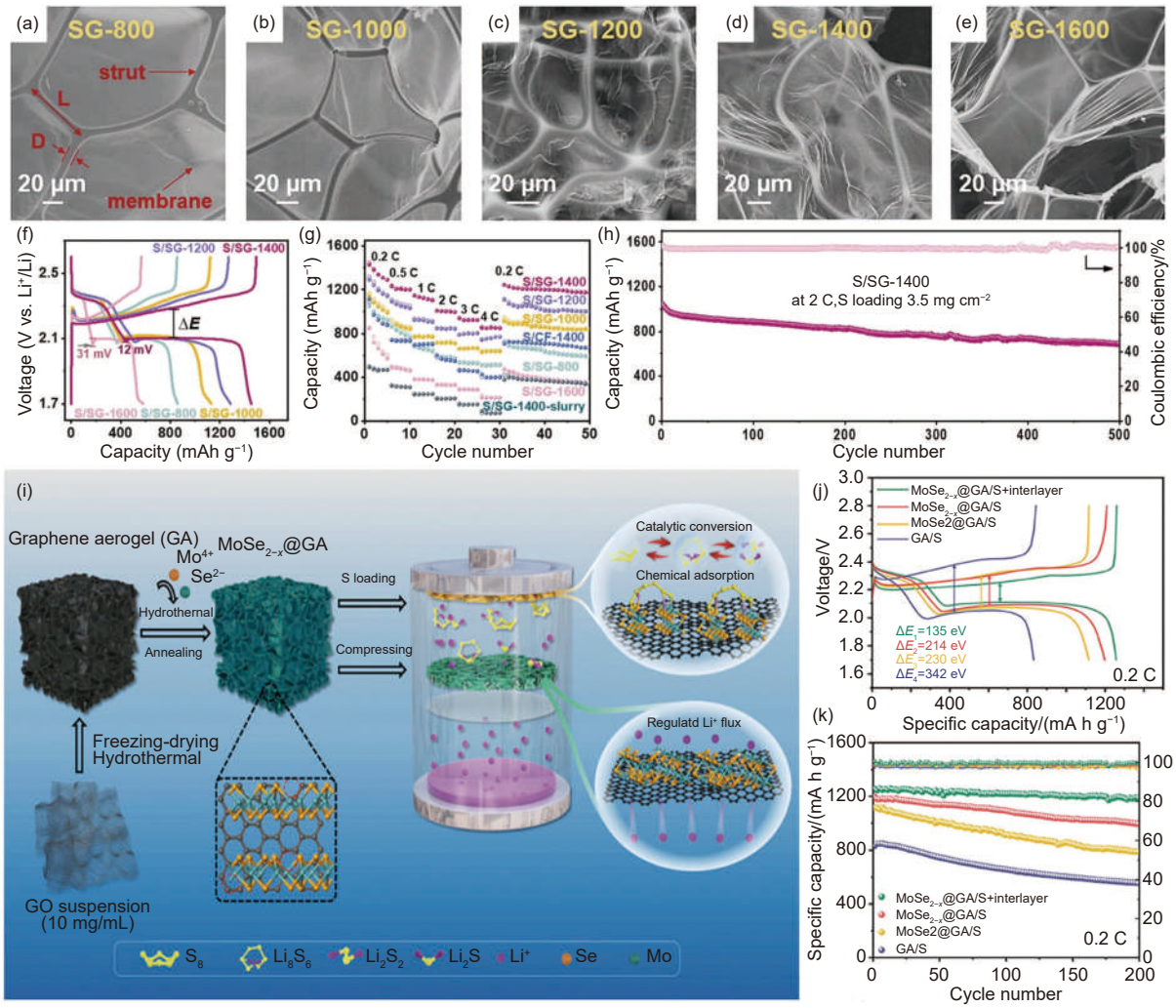

Fig. 18 (a-e) SEM images of SG foams obtained at different etching temperatures. Performances of Li-S batteries using S/SG cathodes: (f) GCD profiles at 0.2 C, (g) rate capability and (h) long-term cycling performance of S/SG-1400 cathode at 2 C (Reproduced with permission, Copyright 2024, Elsevier[23]). (i) The mechanism diagram of the $MoSe_{2-x}$@GA/S+interlayer integrated electrode. Electrochemical performance of GA/S, $MoSe_2$@GA/S, $MoSe_{2-x}$@GA/S and $MoSe_{2-x}$@GA/S+interlayer electrodes: (j) GCD curves (k) cycling performance at 0.2 C; (l) Long-term cycle performance at 1 C for 1000 cycles (Reproduced with permission, Copyright 2023, John Wiley and Sons[153])

(1320 mAh g^{-1}), rate performance (804 mAh g^{-1} at 3C), and cycling stability (0.05% capacity decay per cycle over 500 cycles). Furthermore, Ye et al.[152] advanced this concept further by engineering CoSe-ZnSe heterojunctions on graphene aerogels to catalyze sulfur conversion. Synchrotron spectroscopy and DFT calculations revealed that charge-redistributed interfaces at the heterojunction lower activation barriers for both Li_2S nucleation and decomposition. The optimized electrode achieved 8.0 mAh cm^{-2} areal capacity at ultra-low electrolyte/sulfur ratio (3 μL mg^{-1}), with 96.3% capacity retention after 1700 cycles (0.027% decay/cycle). The hierarchical pore structure concurrently enhanced ion transport kinetics and buffered volume changes during cycling. In addition, holistic cell engineering further boosts Li-S battery efficiency. Zhai et al.[153] designed molybdenum selenide ($MoSe_{2-x}$)-modified graphene aerogels with selenium vacancies to function as both a cathode host ($MoSe_{2-x}$@GA/S) and freestanding interlayers ($MoSe_{2-x}$@GA) for Li-S batteries (Fig. 18i). The binder-free sulfur host supported by the graphene network enhances electron conductivity and lithium-ion migration, while also reducing volumetric expansion. In this modified Li-S battery system, the defect-rich $MoSe_{2-x}$ material, with its sulfur- and lithium-affinitive properties, promotes the nucleation and dissociation of Li_2S. The bifunctional interlayer not only supports the adsorption and conversion of polysulfides but also ensures uniform lithium deposition while preventing the growth of lithium dendrites. As shown in Fig. 18j-l, the $MoSe_{2-x}$@GA/S+ interlayer electrode demonstrated a high initial discharge capacity of 1256.9 mAh g^{-1} at 0.2 C and a lower capacity decay rate of 0.024% per cycle at 1 C after 1000 cycles. Additionally, it achieves a high specific capacity of 720.6 mAh g^{-1} under conditions of high sulfur loading (4.8 mg cm^{-2}) and a lean electrolyte (5.5 μL mg^{-1}).

8.3 Metal-air battery

In addition to the aforementioned battery systems, 3D graphene-based composites are also being explored for using in metal-air batteries. Among these, Li-O_2 batteries stand out due to their exceptionally high energy density and the easy availability of oxygen. Qin et al.[154] developed porous graphene monolith (THPGM) cathodes for Li-O_2 batteries using a high-density template-assisted method. GO serves as the main building block to form condensed carbon electrodes through self-assembly, followed by capillary drying. Then, SiO_2 nanoparticles are added to the dense graphene monolith to act as sacrificial pore formers. This process creates bimodal pores, with diameters of 1-6 nm and approximately 40 nm, within the tightly packed graphene monolith. These pores enhance ion transport and oxygen diffusion while providing ample space for the discharge products. This unique structure results in high volumetric energy densities and excellent cycling stability for Li-O_2 batteries. Additionally, Lacey et al.[155] reported the synthesis of a highly porous 2D nanomaterial (hGO) directly from holey graphene powder, which was then used to create an aqueous ink suitable for 3D printing. The shear-thinning behavior of the aqueous hGO ink allowed for extrusion-based printing of fine filaments into complex 3D structures (Fig. 19a). The 3D-printed hGO meshes displayed trimodal porosity: nanoscale (4-25 nm holes in the hGO sheets), microscale (pores created by lyophilization), and macroscale (large pores within the mesh structure), all of which contributed to the performance enhancement in energy storage devices that rely on interfacial reactions for maximizing active-site utilization. When used as cathodes in Li-O_2 batteries, these 3D printed hGO meshes demonstrate ultrahigh capacity and energy efficiency by catalyzing the reversible formation of Li_2O_2 (Fig. 19b, c). In a new approach for CO_2 sequestration and environmental remediation, the use of CO_2 in Li-CO_2 batteries, which have a high theoretical specific capacity, has recently gained significant attention[156–158]. Hu et al.[159] developed a highly efficient cathode catalyst by implanting single iron atoms into 3D porous carbon architectures for rechargeable Li-CO_2 batteries. The 3D hierarchical architecture of the catalyst, with its large surface area and ample space within the interconnected framework, facilitates electron transport and CO_2/Li^+

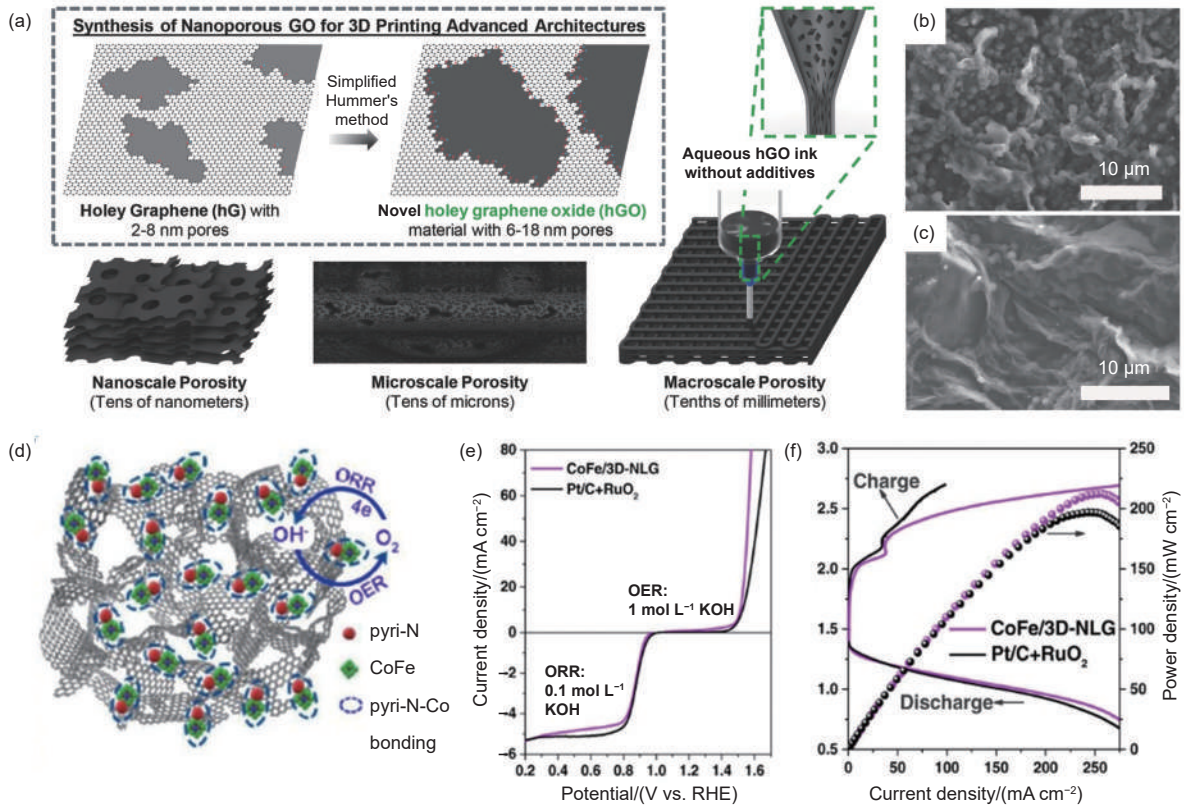

Fig. 19 (a) Schematic representation of 3D printable hGO ink for 3D architectures with hierarchical porosity. SEM images of disassembled r-hGO mesh cathodes in (b) discharge and (c) charge state (Reproduced with permission, Copyright 2018, John Wiley and Sons[155]). (d) Schematic illustration for CoFe/3D-NLG catalyst. (e) The overall polarization curves of CoFe/3D-NLG, CoFe/NG, and Pt/C + RuO_2, measured in O_2-saturated 1.0 mol L^{-1} KOH solution. (f) GCD profiles and power density curves (Reproduced with permission, Copyright 2021, Elsevier[160])

diffusion. It also enables a high uptake of Li_2CO_3, ensuring a high capacity. As a result, the rechargeable Li-CO_2 batteries exhibit a low potential gap of about 1.17 V at 100 mA g^{-1} and can be charged and discharged for over 200 cycles, maintaining a cut-off capacity of 1000 mAh g^{-1} at a high current density of 1 A g^{-1}.

Rechargeable zinc-air batteries are among the most promising energy storage technologies due to their high power density, low cost, environmental friendliness, and safety[19]. In addition to requiring efficient bifunctional catalysis for both oxygen reduction reaction (ORR) and oxygen evolution reaction (OER), the air electrode must also support rapid mass transport. Zhou et al.[160] reported a 3D porous graphene framework (CoFe/3D-NLG) with interconnected macropores and mesopores, enriched with pyridinic-nitrogen-cobalt active sites. As shown in Fig. 19d, the pyridinic-N-Co bonding significantly accelerates the slow oxygen electrocatalysis process, while the large macropores and mesopores within the structure enable highly efficient mass transfer throughout the graphene framework. This robust structure enhances the CoFe/3D-NLG's performance for reversible oxygen electrocatalysis, achieving an ORR half-wave potential comparable to the Pt/C catalyst and an OER activity that surpasses the RuO_2 catalyst (Fig. 19e, f). When used as the air electrode in a rechargeable Zn-air battery, CoFe/3D-NLG exhibits a high open-circuit voltage of 1.56 V, a peak power density of 213 mW cm^{-2}, and a low charge/discharge voltage of 0.63 V. Furthermore, to address the low conductivity and poor understanding of active phase distribution in self-assembled graphene aerogels (GA) in the liquid phase, Hu et al.[161] introduced a simple method that integrates 1D silver nanowires (Ag NWs) during the gelation of GO flakes. The Ag NWs prevent the restacking of graphene sheets and serve as an efficient electron pathway and silver source for the deposition of ultrasmall Ag nanocrystals. When applied

as the cathodic electrocatalyst in a Zn-air battery, the 3D GA integrated with Ag NCs and Ag NWs allows for ultra-high discharge rates up to 300 mA cm^{-2}.

9 Chemical fuel production and conversion based on 3D graphene

An electrocatalytic reaction involves several key steps: (1) reactants diffuse to the catalyst surface; (2) reactants adsorb onto the catalyst surface; (3) electrons are transferred to the catalyst surface; (4) the adsorbed reactants capture electrons to form products. The 3D continuous structure of graphene provides excellent electrical conductivity, which facilitates efficient electron transport. Its large specific surface area offers numerous active sites for rapid charge transfer during catalytic reactions. The open, porous structure promotes efficient mass transport, allowing reactants to easily reach the active sites on the internal surfaces. Additionally, the tunable porosity and chemistry of 3D graphene allow for the optimization of its electronic structure, enhancing its catalytic activity and selectivity for specific reactions.

9.1 Hydrogen evolution reaction (HER)

Water splitting, which involves both the HER and the OER, is a promising method for clean and efficient production of H_2 and O_2. It plays a critical role in addressing the global energy crisis and environmental pollution[162–163]. Electrocatalysts are needed to enhance the reaction rates of both processes. Over the past decade, platinum (Pt) and its alloys have been the most widely used catalysts. However, due to their limited availability and high cost, the use of Pt has slowed the large-scale development and commercialization of water splitting technology[163]. As a result, there has been significant interest in finding low-cost alternatives, such as earth-abundant metals, metal oxides, and metal-free carbon-based materials[163–165]. Among these, 3D nanoporous graphene has been extensively studied for water splitting reactions due to its unique properties. The interconnected, hierarchical structure of 3D graphene also makes it an excellent support for catalyst loading in electrocatalytic water splitting.

The HER is the cathodic process in electrocatalytic water splitting and is considered a promising method for producing hydrogen energy in the future[37]. Significant efforts have been made to develop 3D graphene-based composites as efficient HER electrocatalysts. In Fig. 20a and b, Peng et al.[166] reported a 3D-printed, bioinspired graphene electrode reinforced with 1D carbon nanotubes (3DP GC). This electrode combines high flexural strength with a hierarchical porous structure. The 3DP GC electrode's unique design, with its large surface area and interconnected channels, allows for fast transport of mass, charge and ions (Fig. 20c). Fig. 20d shows that when the 3DP GC electrode is integrated with a NiFeP nanosheet array, it achieves a voltage of 1.58 V at 30 mA cm^{-2} as a bifunctional electrode for water splitting. Furthermore, Luo et al.[167] developed a high-performance electrocatalyst based on a caterpillar-like 3D graphene nanoscroll@CNT (GNS@CNTs) scaffold, decorated with Co-doped $MoSe_2$ nanosheets for HER. In this hierarchical structure, CNTs are seamlessly co-bonded and expand the interlayer and outer spacing of the graphene nanoscrolls through CVD growth. Nickel nanoparticles are then deposited on the tips of the CNTs. Density functional theory calculations show that these nickel nanoparticles can adjust the electronic structure of the Co-doped $MoSe_2$ and improve the ΔG of H* adsorption through electron transfer and doping effects. The hierarchical structure, with its large surface area, high chemical stability, and abundant pores, contributes to the catalyst's high HER efficiency.

9.2 Oxygen evolution reaction (OER)

The OER at the anode used for water splitting generally suffers from slow reaction kinetics due to the four-electron transfer process, which is thermodynamically unfavorable[163]. To overcome this, efficient catalysts are required. 3D graphene, with its large surface area and customizable surface chemistry, along with heteroatom-doped 3D graphene materials (GMs), shows great potential as OER electrocatalysts. Zhu et al.[168] reported a self-supported, highly porous nitro-

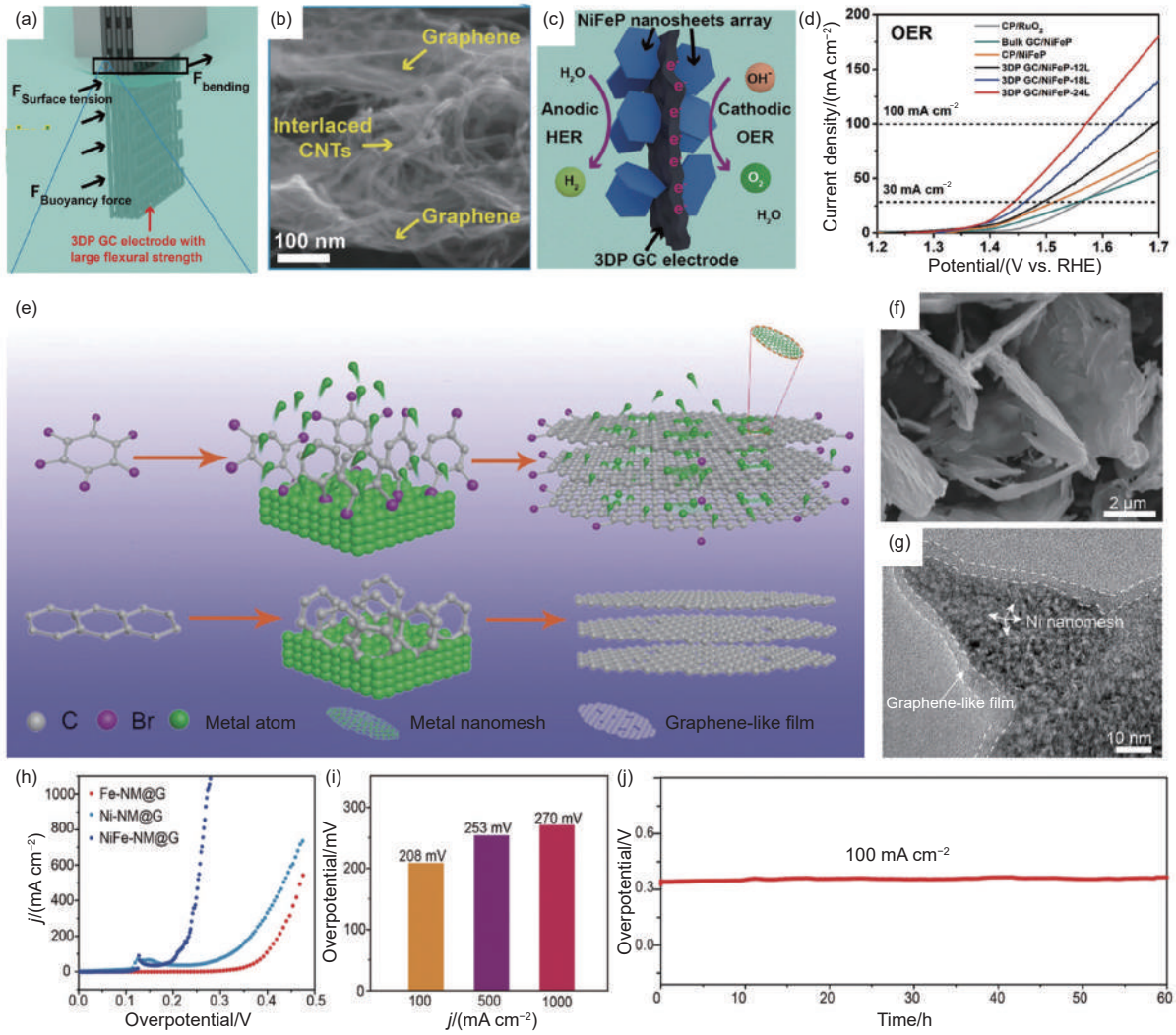

Fig. 20 (a) Schematic illustration shows 3DP GC electrode can withstand the large bending force caused by the surface tension and buoyancy when immersed in water. (b) SEM image of graphene/interlaced CNT nanostructure. (c) Schematic diagram of 3DP GC/NiFeP electrode facilitated ion and gas transport. (d) OER polarization curves of 3DP GC/NiFeP (Reproduced with permission, Copyright 2020, John Wiley and Sons[166]). (e) Scheme of solid-phase migration process for forming M-NM@G catalyst. (f) SEM images and (g) TEM imageof Ni-NM@G-10 catalyst. (h) OER polarization curves in deaerated 1.0 mol L^{-1} KOH solution at a scan rate of 2.0 mV s^{-1}. (i) Comparison of overpotentials at different current densities. (j) Time-dependent current density curve for NiFe-NM@G in 1.0 mol L^{-1} KOH (Reproduced with permission, Copyright 2020, John Wiley and Sons[170])

gen-doped graphene foam, created by electrochemically expanding carbon-fiber paper and then treating it with nitrogen plasma. The foam features well-developed porous structures and uniform nitrogen doping, which enhances the active sites, increases the active surface area, and improves mass and electron transport within the graphene framework. This design leads to excellent performance for electrocatalyzing OER in alkaline media, with a sharp onset potential, low Tafel slope, and impressive durability.

Compared to metal-free heteroatom-doped 3D graphene, 3D graphene-based composites have gained more attention for their higher catalytic activity in the OER. Zhang et al.[169] introduced a new and efficient method to prepare $NiFe_2O_4$ supported on a 3D graphene network (NFO/3DGN) electrocatalyst. In their process, NiFe layered double hydroxide (NiFe LDH) was first exfoliated into single layers using polylactic acid (PLA). When PLA was hydrolyzed, the single-layer NiFe LDH was released, and the PLA hydrolysate helped convert it to $NiFe_2O_4$. Meanwhile, GO was reduced to form 3DGN, which provided a support structure for $NiFe_2O_4$, preventing its agglomeration and creating efficient electron pathways. Theoretical calculations showed that the reaction energy barrier for $NiFe_2O_4$ was significantly lowered due to

the presence of 3DGN. As a result, the NFO/3DGN-10 catalyst demonstrated excellent electrocatalytic activity and stability for OER in alkaline media, with a low overpotential of 272 ± 25 mV at 10 mA cm^{-2} and a Tafel slope of 64 mV dec^{-1}. Besides, Zhang et al.[170] discovered that the organic small molecule hexabromobenzene (HBB) can activate transition metal foam by directly forming metal nanomeshes embedded in graphene-like films (M-NM@G) through a simple Br-induced solid-phase migration process (Fig. 20e). During this process, HBB generated a graphene-like network on the bulk metal foam substrate by cleaving C—Br bonds and forming C—C linkages. The cleaved C—Br fragments efficiently extracted metal atoms from the substrate, in situ forming transition metal nanomeshes embedded in the graphene-like films (Fig. 20f, g). When NiFe foam was used as the substrate, the resulting NiFe-NM@G catalyst showed excellent OER performance, with a low overpotential of only 208 mV at 100 mA cm^{-2} and remarkable long-term stability (Fig. 20h-j).

9.3 Oxygen reduction reaction (ORR)

In the ORR, oxygen interacts with electrons and protons to produce either water (H_2O) by absorbing four electrons or hydrogen peroxide (H_2O_2) by absorbing two electrons. These reactions play a crucial role in many electrochemical devices, including fuel cells and metal-air batteries. Currently, Pt-based catalysts are used for ORR, but they are expensive and prone to deactivation. This issue limits the widespread use of ORR-based devices. Therefore, finding efficient and cost-effective ORR electrocatalysts is essential. 3D graphene is an attractive candidate due to its high specific surface area, fast electron transfer, excellent mechanical strength, and porous structure, which offer good contact and stability for ORR. Zhao et al.[171] fabricated nitrogen-doped, 3D porous graphene frameworks (NGAs) using a novel supramolecular assembly method (Fig. 21a). In this approach, GO served as the building block, and a supramolecular aggregate of self-assembled melamine and cyanuric acid acted both as a spacer to prevent graphene sheets from re-stacking and as a pore-forming agent and nitrogen source for doping. The resulting metal-free NGAs exhibit a high surface area, a porous structure, and good anti-stacking properties, leading to improved ORR performance. Their half-wave potential is only about 43 mV lower than that of commercial Pt/C (Fig. 21b, c).

In addition to metal-free 3D graphene, 3D graphene composites with abundant transition metals have gained more attention due to their higher catalytic activity for the ORR. As shown in Fig. 21d, Zhou et al.[172] reported a negative pressure pyrolysis method to create dense single metal sites (Co, Fe, Ni, etc.) that are highly accessible and dispersed on 3D graphene frameworks. These 3D GFs exhibited improved mesoporosity and external surface area, greatly enhancing the mass transport and metal site utilization. This design contributed to excellent ORR performance (Fig. 21e), with a half-wave potential of 0.901 V vs. RHE. Theoretical calculations also confirmed that selective carbon cleavage near Co centers lowers the overall ORR theoretical overpotential compared to the intact atomic configuration. M-N_x structures are identified as the most active catalytic sites. However, the exact nature of these active sites remains unclear, limiting the understanding of the structure-performance relationship[173]. Huang et al.[174] synthesized a 3D graphene aerogel (GA) supported FeN_5 composite with a well-defined 5-coordinated Fe-N bond. In this composite, pyridine groups were covalently attached to the graphene surface to anchor iron phthalocyanine (FePc) molecules (FePc/AP-GA). The ORR performance of this catalyst showed a half-wave potential of −0.035 V (vs. Hg/HgO) in an alkaline electrolyte. The FePc/AP-GA composite also demonstrated a high kinetic current density of 20 mA cm^{-2} at −0.1 V, excellent durability, and good tolerance to methanol poisoning. X-ray absorption spectroscopy indicated that the geometric and electronic structure of the iron atom in the FePc/AP-GA composite enhances the adsorption of O_2 and intermediates, thereby improving both ORR activity and durability.

9.4 Carbon dioxide reduction reactions (CO_2RR)

In addition to water splitting and the ORR, 3D

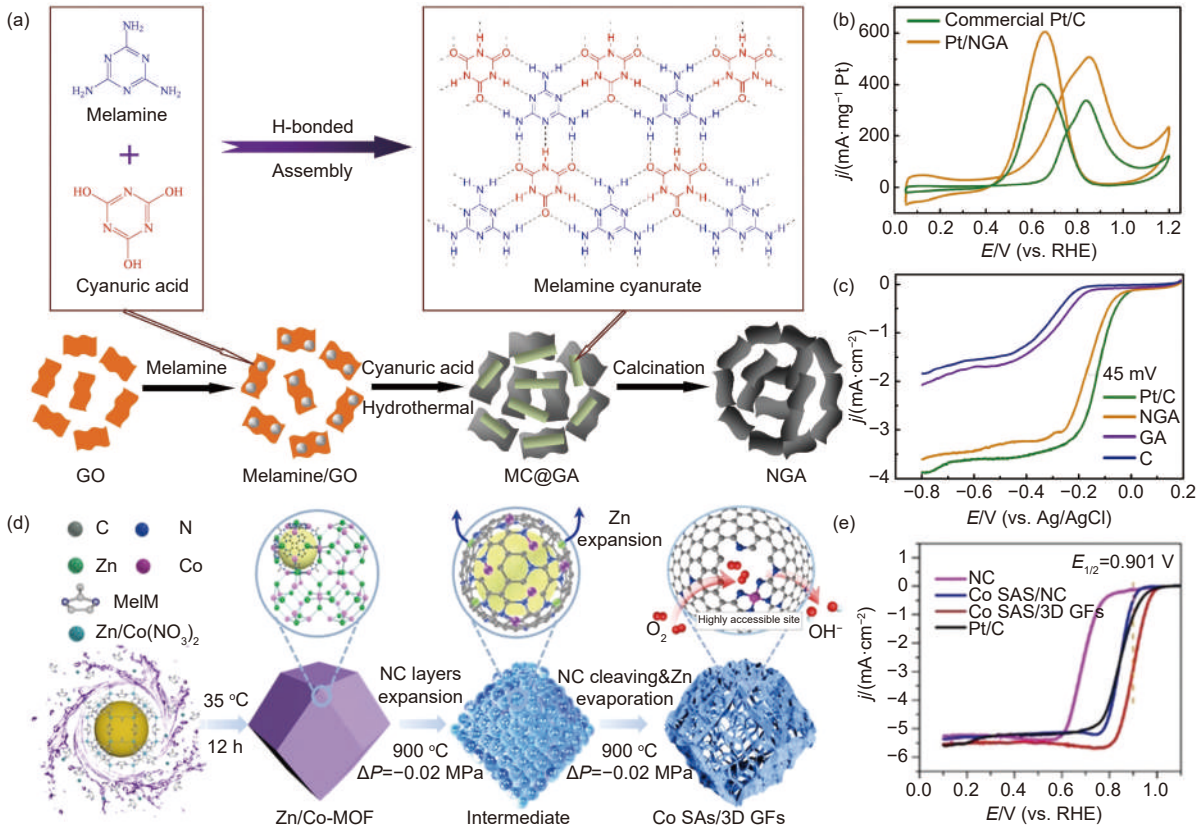

Fig. 21 (a) The synthesis of NGA. (b) Chronoamperometric curves of NGA and commercial Pt/C. (c) Nyquist plots of EIS for Pt/NGA and commercial Pt/C catalysts (Reproduced with permission, Copyright 2018, Elsevier[171]). (d) The synthetic procedure of Co SAs/3D GFs. (e, f) TEM images of Co SAs/3D GFs. (g) LSV curves of Co SAs/3D GFs (Reproduced with permission, Copyright 2020, John Wiley and Sons[172])

graphene has also been studied for CO_2RR. CO_2RR is a promising approach to reduce CO_2 levels and produce valuable fuels and chemicals, addressing both energy and environmental challenges. However, CO_2RR is slow due to the high stability and chemical inertness of CO_2, requiring catalysts to drive the reaction. Moreover, CO_2 can be converted into various products through different electron transfer processes, so choosing catalysts with high selectivity and yield is crucial. 3D graphene's unique structural properties make it an effective catalyst for these reactions. Choi et al.[175] introduced a 3D iron porphyrin-based graphene hydrogel (FePGH) as an electrocatalyst for highly efficient CO_2 reduction to CO. In aqueous medium, FePGH exhibited a highly porous, conductive 3D structure, leading to a faradaic efficiency of about 96.2% for CO production at a low overpotential of 280 mV. Additionally, FePGH demonstrated excellent durability, maintaining a stable CO yield (96.4% FE) over 20 h of electrolysis at the same overpotential, with a high cathodic energy efficiency of 79.7%. Since defects on the graphene surface significantly affect its activity, much attention has been given to creating and optimizing these defects. Ma et al.[176] developed a defective 3D vertical graphene (VG) with a large surface area, high defect density, and increased surface electron density. This was synthesized using a scalable plasma-enhanced CVD method, followed by an Ar-plasma treatment (VG-Ar). Additionally, Cu@Cu_xO nanoparticles were deposited on VG-Ar (Cu/VG-Ar) through galvanostatic pulsed electrodeposition. Cu/VG-Ar achieved a high CO_2 reduction Faradaic efficiency of 60.6%, with 83.5% of the products being liquid (formate, ethanol, and n-propanol), and a current density of 5.6 mA cm^{-2} at −1.2 V vs. RHE. The improved CO_2 reduction performance of Cu/VG-Ar was attributed to the well-dispersed Cu@Cu_xO nanoparticles on the defective VG-Ar. The carbon defects on VG-Ar help suppress the hydrogen evolution reaction and modulate the interaction

between VG and Cu@Cu_xO, preventing excessive oxidation of Cu_2O species. Thus, the defective VG-Ar and stabilized Cu@Cu_xO enhanced CO_2 adsorption, promoted electron transfer to adsorbed CO_2 and intermediates, and improved overall CO_2 reduction performance.

To improve the selectivity and yield of 3D graphene materials (GMs) for CO_2RR, particularly for multicarbon products, an effective approach is to combine them with suitable active species. Recently, Yap et al.[177] investigated the role of lanthanide oxides, specifically CeO_2, in enhancing Cu-based catalytic performance. By utilizing the unique electronic structure of Ce, CO* species are stabilized during the reaction in CeO_2-Cu_2O, leading to excellent catalytic performance for CO_2 electroreduction to C_2 products. Additionally, incorporating CeO_2-Cu_2O with graphene aerogel increases the electrochemical active surface area and boosts CO_2RR efficiency. The resulting CeO_2-Cu_2O(10%)/GA electrocatalyst showed remarkable faradaic efficiency for C_2 products, exceeding 62%, along with excellent stability over 80 h with a wide potential window (−0.8 to −1.2 V) in an H-cell setup. Moreover, when integrated into a solar cell-powered CO_2 reduction system, it maintained stable performance (−27.8 mA cm^{-2} at 3.46 V) under solar radiation of approximately 100 mW cm^{-2}, with nearly 100% efficiency retention over 4 h of continuous illumination. In another approach, Ag nanoparticles were anchored onto 3D graphene-wrapped nitrogen-doped carbon foam (Ag-G-NCF) through direct carbonization of melamine foam loaded with GO and silver salt[178]. This Ag-G-NCF catalyst efficiently converts CO_2 to ethanol, achieving faradaic efficiencies of 82.1%-85.2% at −0.6 to −0.7 V (vs. RHE), overcoming the typical limitations of low faradaic efficiency and selectivity for C_2 products. Density functional theory calculations revealed that the pyridinic N species in Ag-G-NCF have a stronger binding ability with CO* intermediates compared to other nitrogen species, enabling the Ag particles to convert CO* to the ethanol intermediate, OC—COH.

10 Summary and outlook

3D graphene materials, formed by folding atomically thin graphene sheets into a 3D structure, are considered a promising way to address some limitations of 2D graphene, such as sheet restacking and restricted active site accessibility. Meanwhile, 3D graphene retains key properties of graphene-high electrical and thermal conductivities, large surface area, mechanical strength, flexibility, efficient light absorption, and unique 2D electronic behaviors. The interconnected porous networks in 3D graphene may also provide improved mass transport channels, open internal space, and low mass density.

As summarized in Fig. 22, this review outlines recent developments in fabrication methods, structure-property relationships, and selected applications of 3D graphene in energy storage and conversion. 3D graphene is mainly synthesized by CVD, GO assembly, 3D printing, chemical blowing, and zinc-tiered pyrolysis. CVD yields high-quality frameworks with good conductivity. GO self-assembly methods, such as hydrothermal reduction and ice templating, are scalable and low-cost. Techniques like 3D printing offer control over hierarchical structures for customized applications. Alternative approaches such as laser-induced synthesis and chemical blowing can further expand the options for tuning porosity and surface chemistry. These diverse methods continue to support 3D graphene's potential in energy-related applications.

3D graphene has been studied in areas such as mechanical energy absorption and acoustic damping. In PCMs, it may help improve thermal conductivity, photothermal performance, and mechanical stability. Its 3D structure can also reduce impedance mismatch in electromagnetic applications, enhancing microwave absorption. In supercapacitors, its high surface area and hierarchical porosity facilitate ion transport with reduced resistance. For ion batteries, 3D graphene serves as a conductive scaffold hosting active materials, potentially improving cycling stability. In metal-air batteries, 3D graphene frameworks with catalytic sites have shown promising power output

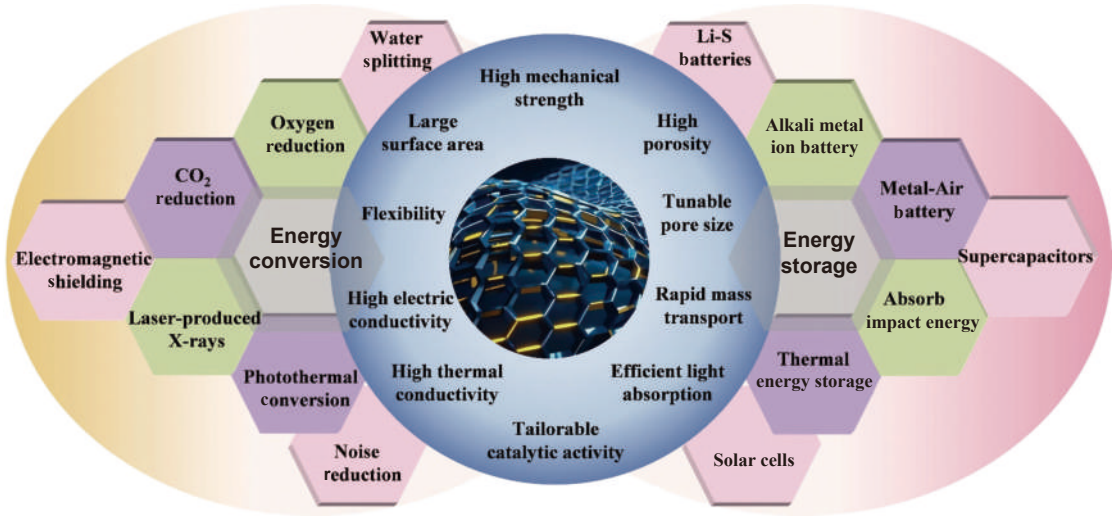

Fig. 22 Summary of remarkable properties of 3D graphene materials and advancing applications of energy storage and conversion

and durability. In water splitting, nitrogen-doped graphene foams and hybrids have demonstrated low overpotentials and reasonable faradaic efficiency.

Although progress has been made, the concept of the ideal 3D graphene remains under exploration. Scalable, low-cost, and environmentally friendly fabrication methods would be beneficial. Tailoring pore distribution, heteroatom doping, and curvature could help optimize transport and interfacial behavior.

In summary, 3D graphene offers structural advantages that may help bridge nanoscale material properties with practical energy device needs. Continued development in synthesis and integration could support its future role in sustainable, efficient energy systems.

Credit authorship contribution statement

WU Zi-yuan: Writing original draft, Methodology, Investigation. XU Chi-wei: Writing review & editing, Methodology. ZENG Jin-jue: Writing review & editing. JIANG Xiang-fen: Writing review & editing, Supervision. WANG Xue-bin: Writing review & editing.

Declaration of competing interest

The authors declare that they have no known competing financial interests or personal relationships that could have appeared to influence the work reported in this paper.

Acknowledgements

This work is supported by National Natural Science Foundation of China (52272039, U23B2075, 51972168), Key Research and Development Program in Jiangsu Province (BE2023085), Natural Science Foundation of Jiangsu Province of China (BK20231406), and Center for Microscopy and Analysis of Nanjing University of Aeronautics and Astronautics.

References

[1] Novoselov K, Geim A, Morozov S, et al. Electric field effect in atomically thin carbon films[J]. Science, 2004, 306(5696): 666-669.

[2] Morozov S, Novoselov K, Katsnelson M, et al. Giant intrinsic carrier mobilities in graphene and its bilayer[J]. Physical Review Letters, 2008, 100(1): 016602.

[3] Bolotin K, Sikes K, Jiang Z, et al. Ultrahigh electron mobility in

suspended graphene[J]. Solid State Communiacations, 2008, 146(9-10): 351-355.
[4] Balandin A, Ghosh S, Bao W, et al. Superior thermal conductivity of single-layer graphene[J]. Nano Letters, 2008, 8(3): 902-907.
[5] Lee C, Wei X, Kysar J, et al. Measurement of the elastic properties and intrinsic strength of sonolayer graphene[J]. Science, 2008, 321(5887): 385-388.
[6] Novoselov K, Jiang Z, Zhang Y, et al. Room-temperature quantum hall effect in graphene[J]. Science, 2007, 315(5817): 1379.
[7] Zhang Y, Tan Y, Stormer H, et al. Experimental observation of the quantum hall effect and berry's phase in graphene[J]. Nature, 2005, 438(7065): 201-204.
[8] Jiang Z, Zhang Y, Stormer H, et al. Quantum hall states near the charge-neutral dirac point in graphene[J]. Physical Review Letters, 2007, 99(10): 106802.
[9] Schedin F, Geim A, Morozov S, et al. Detection of individual gas molecules adsorbed on graphene[J]. Nature Materials, 2007, 6(9): 652-655.
[10] Xu C, Zeng J, Wang Y, et al. Graphene and boron nitride foams for smart functional applications[J]. SmartMat, 2023, 4(4): e1199.
[11] Yun Q, Ge Y, Chen B, et al. Hybridization of 2D Nanomaterials with 3D graphene architectures for electrochemical energy storage and conversion[J]. Advanced Functional Materials, 2022, 32(42): 2202319.
[12] Ye R, James D, Tour J, Laser-induced graphene: from discovery to translation[J]. Advanced Materials, 2019, 31 (1) : 1803621.
[13] Qi Y, Xia Y, Li P, et al. Plastic-swelling preparation of functional graphene aerogel fiber textiles[J]. Advanced Fiber Materials, 2023, 5(6): 2016-2027.
[14] Wang Y, Wei T, Wang Y, et al. Quasi-waffle solar distiller for durable desalination of seawater[J]. Science Advances, 2024, 10(22): e1113.
[15] Zeng J, Wang T, Wang Y, et al. Large-surface-area porous monolith of graphene for electrochemical capacitive deionization[J]. Journal of Materials Chemistry A, 2023, 11(43): 23430-23437.
[16] Duan W, Sun Z, Jiang X, et al. Carbon materials for evaporation- and moisture-induced power generation[J]. Nano Energy, 2025, 134: 110516.
[17] Guan T, Li Z, Qiu D, et al. Recent progress of graphene fiber/fabric supercapacitors: from building block architecture, fiber assembly, and fabric construction to wearable applications[J]. Advanced Fiber Materials, 2023, 5(3): 896-927.
[18] Zhu Z, Men Y, Zhang W, et al. Versatile carbon-based materials from biomass for advanced electrochemical energy storage systems[J]. eScience, 2024, 4(5): 100249.
[19] Han J, Johnson I, Chen M, 3D continuously porous graphene for energy applications[J]. Advanced Materials, 2022, 34 (15) : 2108750.
[20] Wang H, Mi X, Li Y, et al. 3D graphene-based macrostructures for water treatment[J]. Advanced Materials, 2020, 32(3): 1806843.
[21] Sun Z, Fang S, Hu Y, 3D graphene materials: from understanding to design and synthesis control[J]. Chemical Reviews, 2020, 120 (18) : 10336-10453.
[22] Xu Y, Sheng K, Li C, et al. Self-assembled graphene hydrogel via a one-step hydrothermal process[J]. ACS Nano, 2010, 4(7): 4324-4330.
[23] Zhou F, Meng Y, Wang T, et al. Strutted graphene foam loading sulfur for high-rate long-lifetime Li-S batteries[J]. Nano Energy, 2024, 127: 109755.
[24] Chabot V, Higgins D, Yu A, et al. A review of graphene and graphene oxide sponge: material synthesis and applications to energy and the environment[J]. Energy & Environmental Science, 2014, 7(5): 1564-1596.
[25] Zeng J, Ji X, Ma Y, et al. 3D graphene fibers grown by thermal chemical vapor deposition[J]. Advanced Materials, 2018, 30(12): 1705380.
[26] Ito Y, Tanabe Y, Qiu H, et al. High-quality three-dimensional nanoporous graphene[J]. Angewandte Chemie International Edition, 2014, 53(19): 4822-4826.
[27] Zhang Y, Wan Q, Yang N, Recent Advances of porous graphene: synthesis, functionalization, and electrochemical applications[J]. Small, 2019, 15 (48) : 1903780.
[28] Wang X, Zhang Y, Zhi C, et al. Three-dimensional strutted graphene grown by substrate-free sugar blowing for high-power-density supercapacitors[J]. Nature Communications, 2013, 4: 2905.
[29] Lu Y, Ma Y, Zhang T, et al. Monolithic 3D cross-linked polymeric graphene materials and the likes: preparation and their redox catalytic applications[J]. Journal of the American Chemical Society, 2018, 140(37): 11538-11550.
[30] Chen K, Shi L, Zhang Y, et al. Scalable chemical-vapour-deposition growth of three-dimensional graphene materials towards energy-related applications[J]. Chemical Society Reviews, 2018, 47(9): 3018-3036.
[31] Kumar S, Goswami M, Singh N, et al. A comprehensive review of the 3D printing of sp^2 carbons: Materials, properties and applications[J]. New Carbon Materials, 2022, 37(6): 1046-1063.
[32] Zeng J, Xu C, Gao T, et al. Porous monoliths of 3D graphene for electric double-layer supercapacitors[J]. Carbon Energy, 2021, 3(2): 193-224.
[33] Yao X, Zhao Y, Three-dimensional porous graphene networks and hybrids for lithium-ion batteries and supercapacitors[J]. Chem, 2017, 2 (2) : 171-200.
[34] Mao J, Iocozzia J, Huang J, et al. Graphene aerogels for efficient energy storage and conversion[J]. Energy & Environmental Science, 2018, 11(4): 772-799.
[35] Luo S, Samad Y, Chan V, et al. Cellular graphene: fabrication, mechanical properties, and strain-sensing applications[J]. Matter, 2019, 1(5): 1148-1202.
[36] Lang Y, He Y, Song H, et al. Progress in the research of carbon aerogel in photothermal conversion[J]. New Carbon Materials,

2024, 39(6): 1075-1087.

[37] Jing Y, Liu H, Zhou F, et al. Design, progress and challenges of 3D carbon-based thermally conductive networks[J]. New Carbon Materials, 2024, 39(5): 844-871.

[38] Kuang P, Sayed M, Fan J, et al. 3D graphene-based H_2-production photocatalyst and electrocatalyst[J]. Advanced Energy Materials, 2020, 10(14): 1903802.

[39] Cui H, Guo Y, Zhou Z, Three-dimensional graphene-based macrostructures for electrocatalysis[J]. Small, 2021, 17 (22) : 2005255.

[40] Jia H, Liang L, Liu D, et al. A review of three-dimensional graphene networks for thermal management and electromagnetic protection[J]. New Carbon Materials, 2021, 36(5): 851-868.

[41] Sun Z, Yu J, Liu C, et al. Foam materials for applications of electromagnetic shielding and microwave absorption[J]. Materials Research Bulletin, 2024, 180: 113001.

[42] Ni J, Shi Z, Wang Y, et al. Development of noble metal-free electrocatalysts towards acidic water oxidation: from fundamental understanding to state-of-the-art catalysts[J]. eScience, 2025, 5(2): 100295.

[43] Huang S, Wen K, Liu Y, et al. Optimized design, fabrication, and enhanced performance of honeycomb sandwich structure for excellent impact resistance and broadband microwave absorption[J]. Journal of Colloid and Interface Science, 2025, 681: 365-375.

[44] Jin S, Feng Y, Jia J, et al. Three-dimensional N-doped carbon nanotube/graphene composite aerogel anode to develop high-power microbial fuel cell[J]. Energy & Environmental Materials, 2022, 6(3): e12373.

[45] Jiang X, Xu C, Gao T, et al. Flexible conductive polymer composite materials based on strutted graphene foam[J]. Composites Communications, 2021, 25: 100757.

[46] Yan B, Hao C, Meng Q, et al. Asymmetric pt nanoparticles with high lattice strain grown onto 3D graphene film as efficient integrated catalyst layer for proton exchange membrane fuel cells[J]. FlatChem, 2023, 42: 100560.

[47] Wei R, Liu X, Ibragimov A, et al. Recent strategies to improve the electroactivity of metal-organic frameworks for advanced electrocatalysis[J]. Information & Functional Materials, 2024, 1(2): 181-206.

[48] Liu F, Yang Y, Xu M, et al. 2D covalent organic framework/reduced graphene oxide hybrid hydrogel for simultaneous power generation and organic contamination degradation in microbial fuel cell[J]. Materials Today Energy, 2024, 39: 101464.

[49] Pang K, Liu X, Pang J, et al. Highly efficient cellular acoustic absorber of graphene ultrathin drums[J]. Advanced Materials, 2022, 34(14): 2103740.

[50] Zhang Q, Cheng X, Wang C, et al. Sulfur-assisted large-scale synthesis of graphene microspheres for superior potassium-ion batteries[J]. Energy & Environmental Science, 2021, 14(2): 965-974.

[51] Ito Y, Tanabe Y, Sugawara K, et al. Three-dimensional porous graphene networks expand graphene-based electronic device applications[J]. Physical Chemistry Chemical Physics, 2018, 20(9): 6024-6033.

[52] Chen Z, Ren W, Gao L, et al. Three-dimensional flexible and conductive interconnected graphene networks grown by chemical vapour deposition[J]. Nature Materials, 2011, 10(6): 424-428.

[53] Bi H, Lin T, Xu F, et al. New graphene form of nanoporous monolith for excellent energy storage[J]. Nano Letters, 2016, 16(1): 349-354.

[54] Nautiyal P, Mujawar M, Boesl B, et al. In-situ mechanics of 3D graphene foam based ultra-stiff and flexible metallic metamaterial[J]. Carbon, 2018, 137: 502-510.

[55] Li X, Guo J, Theoretical study on uniaxial compressive mechanical properties of three-dimensional graphene[J]. International Journal of Mechanical Sciences, 2023, 249 : 108250.

[56] Bao Q, Yang Z, Lu Z, et al. Effects of graphene thickness and length distribution on the mechanical properties of graphene networks: A coarse-grained molecular dynamics simulation[J]. Applied Surface Science, 2021, 570: 151023.

[57] Liu Z, Zhang W, Yin M, et al. Ion-crosslinking induced dynamic assembly of porous 3D graphene oxide framework for CO_2 capture[J]. Separation And Purification Technology, 2023, 312: 123448.

[58] Zhang X, Li J, Gao Q, et al. Nerve-fiber-inspired construction of 3D graphene “tracks” supported by wood fibers for multifunctional biocomposite with metal-level thermal conductivity[J]. Advanced Functional Materials, 2023, 33(18): 2213274.

[59] Bo Z, Ying C, Yang H, et al. Highly thermo-conductive three-dimensional graphene aqueous medium[J]. Nano-Micro Letters, 2020, 12(1): 138.

[60] Huang P, Ruiz-Vargas C, Zande A, et al. Grains and grain boundaries in single-layer graphene atomic patchwork quilts[J]. Nature, 2011, 469(7330): 389-392.

[61] Tanabe Y, Ito Y, Sugawara K, et al. Dirac fermion kinetics in 3D curved graphene[J]. Advanced Materials, 2020, 32(48): 2005838.

[62] Tanabe Y, Ito Y, Sugawara K, et al. Coexistence of urbach-tail-like localized states and metallic conduction channels in nitrogen-doped 3D curved graphene[J]. Advanced Materials, 2022, 34(51): 2205986.

[63] Stankovich S, Dikin D, Piner R, et al. Synthesis of graphene-based nanosheets via chemical reduction of exfoliated graphite oxide[J]. Carbon, 2007, 45(7): 1558-1565.

[64] Liu F, Seo T, A controllable self-Assembly method for large-scale synthesis of graphene sponges and free-standing graphene films[J]. Advanced Functional Materials, 2010, 20 (12) : 1930-1936.

[65] Gao W, Singh N, Song L, et al. Direct laser writing of micro-supercapacitors on hydrated graphite oxide films[J]. Nature Nanotechnology, 2011, 6(8): 496-500.

[66] Zhu C, Han T, Duoss E, et al. Highly compressible 3D periodic graphene aerogel microlattices[J]. Nature Communications, 2015, 6: 6962.
[67] El-Kady M, Strong V, Dubin S, et al. Laser scribing of high-performance and flexible graphene-based electrochemical capacitors[J]. Science, 2012, 335(6074): 1326-1330.
[68] Jiang X, Li R, Hu M, et al. Zinc-tiered synthesis of 3D graphene for monolithic electrodes[J]. Advanced Materials, 2019, 31(25): 1901186.
[69] Pan F, Chen S, Li Y, et al. 3D graphene films enable simultaneously high sensitivity and large stretchability for strain sensors[J]. Advanced Functional Materials, 2018, 28(40): 1803221.
[70] Gao T, Xu C, Li R, et al. Biomass-derived carbon paper to sandwich magnetite anode for long-life li-ion battery[J]. ACS Nano, 2019, 13(10): 11901-11911.
[71] Zhang P, Li J, Lv L, et al. Vertically aligned graphene sheets membrane for highly efficient solar thermal generation of clean water[J]. ACS Nano, 2017, 11(5): 5087-5093.
[72] Choi B, Yang M, Hong W, et al. 3D macroporous graphene frameworks for supercapacitors with high energy and power densities[J]. ACS Nano, 2012, 6(5): 4020-4028.
[73] Chen K, Song S, Xue D, Beyond graphene: materials chemistry toward high performance inorganic functional materials[J]. Journal of Materials Chemistry A, 2015, 3 (6) : 2441-2453.
[74] Qiu L, Liu J, Chang S, et al. Biomimetic superelastic graphene-based cellular monoliths[J]. Nature Communications, 2012, 3: 1241.
[75] Farahani R, Dube M, Therriault D, Three-dimensional printing of multifunctional nanocomposites: manufacturing techniques and applications[J]. Advanced Materials, 2016, 28 (28) : 5794-5821.
[76] Garcia-Tunon E, Barg S, Franco J, et al. Printing in three dimensions with graphene[J]. Advanced Materials, 2015, 27(10): 1688-1693.
[77] Ma J, Wang P, Dong L, et al. Highly conductive, mechanically strong graphene monolith assembled by three-dimensional printing of large graphene oxide[J]. Journal of Colloid and Interface Science, 2019, 534: 12-19.
[78] Chen Q, Shen J, Estevez D, et al. Ultraprecise 3D printed graphene aerogel microlattices on tape for micro sensors and E-skin[J]. Advanced Functional Materials, 2023, 33(33): 2302545.
[79] Xu X, Du J, Cao Q, et al. Digitization of free-shapable graphene foam with damage tolerance[J]. Advanced Functional Materials, 2023, 33(21): 2300904.
[80] Zhang Q, Zhang F, Xu X, et al. Three-dimensional printing hollow polymer template-mediated graphene lattices with tailorable architectures and multifunctional properties[J]. ACS Nano, 2018, 12(2): 1096-1106.
[81] Ma X, Zachariah M, Zangmeister C, Crumpled nanopaper from graphene oxide[J]. Nano Letters, 2012, 12 (1) : 486-489.
[82] Yang H, Li Z, Sun G, et al. Superplastic air-dryable graphene hydrogels for wet-press assembly of ultrastrong superelastic aerogels with infinite macroscale[J]. Advanced Functional Materials, 2019, 29(26): 1901917.
[83] Feng J, Safaei B, Qin Z, et al. Bio-inspired metallic cellular material with extraordinary energy dissipation capability[J]. Chemical Engineering Journal, 2023, 475: 146382.
[84] Zhang W, Zhang Y, Zhao S, et al. Ballistic impact induced wave propagation and dislocation of three-dimensional graphene origami/copper nanocomposites[J]. Composites Communications, 2024, 45: 101790.
[85] Ge H, Yang M, Ma C, et al. Breaking the barriers: advances in acoustic functional materials[J]. National Science Review, 2018, 5(2): 159-182.
[86] Nine M, Ayub M, Zander A, et al. Graphene oxide-based lamella network for enhanced sound absorption[J]. Advanced Functional Materials, 2017, 27(46): 1703820.
[87] Zong D, Cao L, Yin X, et al. Flexible ceramic nanofibrous sponges with hierarchically entangled graphene networks enable noise absorption[J]. Nature Communications, 2021, 12(1): 6599.
[88] Zong D, Bai W, Geng M, et al. Direct synthesis of elastic and stretchable hierarchical structured fiber and graphene-based sponges for noise reduction[J]. ACS Nano, 2023, 17(17): 17576-17586.
[89] Wang Q, Domen K, Particulate photocatalysts for light-driven water splitting: mechanisms, challenges, and design strategies[J]. Chemical Reviews, 2020, 120 (2) : 919-985.
[90] Akhiani A, Cornelis M, Ang B, et al. Highly hydrophobic silanized melamine foam for facile and uniform assembly of graphene nanoplatelet towards efficient light-to-thermal energy storage[J]. Materials Today Energy, 2022, 28: 101077.
[91] Irshad M, Arshad N, Asghar M, et al. Advances of 2D-enabled photothermal materials in hybrid solar-driven interfacial evaporation systems toward water-fuel-energy Crisis[J]. Advanced Functional Materials, 2023, 33(51): 2304936.
[92] Hao W, Chiou K, Qiao Y, et al. Crumpled graphene ball-based broadband solar absorbers[J]. Nanoscale, 2018, 10(14): 6306-6312.
[93] Kryuchkov M, Bilousov O, Lehmann J, et al. Reverse and forward engineering of drosophila corneal nanocoatings[J]. Nature, 2020, 585(7825): 383-389.
[94] Peng Y, Zhao W, Ni F, et al. Forest-like laser-induced graphene film with ultrahigh solar energy utilization efficiency[J]. ACS Nano, 2021, 15(12): 19490-19502.
[95] Tian K, Fan X, Cheng S, et al. Graphene microflower by photothermal marangoni-induced fluid instability for omnidirectional broadband photothermal conversion[J]. ACS Nano, 2024, 18(43): 29760-29770.
[96] Liao Q, Zhu K, Hao X, et al. Bio-inspired ultrathin perfect absorber for high-performance photothermal conversion[J]. Advanced Materials, 2024, 36(24): 2313366.
[97] Liu L, Xu C, Yang Y, et al. Graphene-based polymer composites in thermal management: materials, structures and applications[J]. Materials Horizons, 2025, 12(1): 64-91.

[98] Su W, Hu M, Wang L, et al. Microencapsulated phase change materials with graphene-based materials: fabrication, characterisation and prospects[J]. Renewable and Sustainable Energy Reviews, 2022, 168: 112806.

[99] Zhu Q, Ong P, Goh S, et al. Recent advances in graphene-based phase change composites for thermal energy storage and management[J]. Nano Materials Science, 2024, 6(2): 115-138.

[100] Zhu X, Liu J, Yang K, et al. Structurally engineered 3D porous graphene based phase change composite with highly efficient multi-energy conversion and versatile applications[J]. Composites Part B: Engineering, 2024, 272: 111233.

[101] Xi S, Wang L, Xie H, et al. Superhydrophilic modified elastomeric RGO aerogel based hydrated salt phase change materials for effective solar thermal conversion and storage[J]. ACS Nano, 2022, 16(3): 3843-3851.

[102] Liang K, Zhang H, Wang Q, et al. PVA-assisted graphene aerogels composite phase change materials with anisotropic porous structure for thermal management[J]. Carbon, 2024, 230: 119639.

[103] Lin Y, Kang Q, Wei H, et al. Spider web-inspired graphene skeleton-based high thermal conductivity phase change nanocomposites for battery thermal management[J]. Nano-Micro Letters, 2021, 13(1): 180.

[104] Das S, Pandey D, Thomas J, et al. The Role of graphene and other 2D materials in solar photovoltaics[J]. Advanced Materials, 2019, 31(1): 1802722.

[105] Rosli N, Ibrahim M, Ludin N, et al. A review of graphene based transparent conducting films for use in solar photovoltaic applications[J]. Renewable Sustainable Energy Reviews, 2019, 99: 83-99.

[106] Gao Y, Zhong C, Yang S, et al. Three-dimensional acetylenic modified graphene for high-performance optoelectronics and topological materials[J]. npj Computational Materials, 2021, 7(1): 109.

[107] Yao J, Wang W, Zuo X, et al. Multi-interface superstructure strategy to improve the catalytic activity and cyclic stability in enhancing the photo conversion in solar cells[J]. Applied Catalysis B: Environment and Energy, 2019, 256: 117857.

[108] Zhang R, Zhang B, Liu Y, et al. Preparation of 3D graphene networks and a C dot grafted graphene hybrid by new methods for improving the photovoltaic performance of CdS/CdSe quantum dot sensitized solar cells[J]. Journal of Materials Chemistry C, 2016, 4(8): 1633-1644.

[109] Zou H, He B, Kuang P, et al. Ni_xS_y nanowalls/nitrogen-doped graphene foam is an efficient trifunctional catalyst for unassisted artificial photosynthesis[J]. Advanced Functional Materials, 2018, 28(13): 1706917.

[110] Hanmandlu C, Paste R, Tsai H, et al. 3D nanographene precursor suppress interfacial recombination in PEDOT : PSS based perovskite solar cells[J]. Nano Energy, 2023, 107 : 108136.

[111] Bie C, Yu H, Cheng B, et al. Design, fabrication, and mechanism of nitrogen-doped graphene-based photocatalyst[J]. Advanced Materials, 2021, 33(9): 2003521.

[112] Tam T, Bhamu K, Kim M, et al. Engineering phosphorous doped graphene quantum dots decorated on graphene hydrogel as effective photocatalyst and high-current density electrocatalyst for seawater splitting[J]. Chemical Engineering Journal, 2024, 480: 148190.

[113] Maouche C, Zhou Y, Peng J, et al. A 3D nitrogen-doped graphene aerogel for enhanced visible-light photocatalytic pollutant degradation and hydrogen evolution[J]. RSC Advanced, 2020, 10(21): 12423-12431.

[114] Chen F, An W, Liu L, et al. Highly efficient removal of bisphenol A by three-dimensional graphene hydrogel-AgBr@rGO exhibiting adsorption/photocatalysis synergy[J]. Applied Catalysis B: Environment and Energy, 2017, 217: 65-80.

[115] Yan S, Song H, Li Y, et al. Integrated reduced graphene oxide/polypyrrole hybrid aerogels for simultaneous photocatalytic decontamination and water evaporation[J]. Applied Catalysis B: Environment and Energy, 2022, 301: 120820.

[116] Kodama R, Sentoku Y, Chen Z, Plasma devices to guide and collimate a high density of MeV electrons[J]. Nature, 2004, 432 : 1005-1008.

[117] Passoni M, Arioli F, Cialfi L, et al. Advanced laser-driven ion sources and their applications in materials and nuclear science[J]. Plasma Physics and Controlled Fusion, 2019, 62(1): 014022.

[118] Cao L, Gu Y, Zhao Z, et al. Enhanced absorption of intense short-pulse laser light by subwavelength nanolayered target[J]. Physics Plasmas, 2010, 17(4): 043103.

[119] Li X, Yang X, Zhang G, et al. High absorption efficiency by high intensity laser irradiating carbon aerogel targets[J]. Physics Plasmas, 2022, 29(1): 013103.

[120] Nishikawa T, Suzuki S, Watanabe Y, et al. Efficient water-window X-ray pulse generation from femtosecond-laser-produced plasma by using a carbon nanotube target[J]. Applied Physics B: Lasers and Optics, 2004, 78(78): 885-890.

[121] Ji Y, Jiang G, Wu W, et al. Efficient generation and transportation of energetic electrons in a carbon nanotube array target[J]. Applied Physics Letters, 2010, 96(4): 041504.

[122] Zhi D, Li T, Li J, et al. A review of three-dimensional graphene-based aerogels: Synthesis, structure and application for microwave absorption[J]. Composites Part B: Engineering, 2021, 211: 108642.

[123] Peng F, Dai M, Wang Z, et al. Progress in graphene-based magnetic hybrids towards highly efficiency for microwave absorption[J]. Journal of Materials Science and Technology, 2022, 106: 147-161.

[124] Sultanov F, Daulbayev C, Bakbolat B, et al. Advances of 3D graphene and its composites in the field of microwave absorption[J]. Advances in Colloid and Interface Science, 2020, 285: 102281.

[125] Huang M, Wang C, Quan L, et al. CVD growth of porous graphene foam in film form[J]. Matter, 2020, 3(2): 487-497.

[126] Xu J, Li R, Ji S, et al. Multifunctional graphene microstructures

inspired by honeycomb for ultrahigh performance electromagnetic interference shielding and wearable applications[J]. ACS Nano, 2021, 15(5): 8907-8918.

[127] Huang X, Wei J, Zhang Y, et al. Ultralight magnetic and dielectric aerogels achieved by metal-organic framework initiated gelation of graphene oxide for enhanced microwave absorption[J]. Nano-Micro Letters, 2022, 14(1): 107.

[128] Ghaffarkhah A, Hashemi S, Rostami S, et al. Ultra-flyweight cryogels of MXene/graphene oxide for electromagnetic interference shielding[J]. Advanced Functional Materials, 2023, 33(50): 2304748.

[129] Sun D, Sun Z, Yang D, et al. Advances in boron nitride-based materials for electrochemical energy storage and conversion[J]. EcoEnergy, 2023, 1(2): 375-404.

[130] Qin K, Kang J, Li J, et al. Continuously hierarchical nanoporous graphene film for flexible solid-state supercapacitors with excellent performance[J]. Nano Energy, 2016, 24: 158-164.

[131] Li Z, Gadipelli S, Li H, et al. Tuning the interlayer spacing of graphene laminate films for efficient pore utilization towards compact capacitive energy storage[J]. Nature Energy, 2020, 5(2): 160-168.

[132] Li C, Yang J, Pachfule P, et al. Ultralight covalent organic framework/graphene aerogels with hierarchical porosity[J]. Nature Communications, 2020, 11(1): 4712.

[133] Wang S, Wang X, Sun C, et al. Room-temperature fast assembly of 3D macroscopically porous graphene frameworks for binder-free compact supercapacitors with high gravimetric and volumetric capacitances[J]. Journal of Energy Chemistry, 2021, 61: 23-28.

[134] Chen Y, Zhu Y, Sun Z, et al. Achieving high-capacity cathode presodiation agent via triggering anionic oxidation activity in sodium oxide[J]. Advanced Materials, 2024, 36(36): 2407720.

[135] Chen Y, Zhu Y, Zuo W, et al. Implanting transition metal into Li_2O-Based cathode prelithiation agent for high-energy-density and long-life Li-ion batteries[J]. Angewandte Chemie International Edition, 2024, 63(5): 202316112.

[136] Ponrouch A, Goñi A, Palacín M, High capacity hard carbon anodes for sodium ion batteries in additive free electrolyte[J]. Electrochemistry Communications, 2013, 27 : 85-88.

[137] Fan L, Liu Q, Chen S, et al. Soft carbon as anode for high-performance sodium-based dual ion full battery[J]. Advanced Energy Materials, 2017, 7(14): 1602778.

[138] Balogun M, Luo Y, Qiu W, et al. A review of carbon materials and their composites with alloy metals for sodium ion battery anodes[J]. Carbon, 2016, 98: 162-178.

[139] Wang J, Liu J, Chao D, et al. Self-assembly of honeycomb-like MoS_2 nanoarchitectures anchored into graphene foam for enhanced lithium-ion storage[J]. Advanced Materials, 2014, 26(42): 7162-7169.

[140] Lee G, Lee J, Choi J, et al. Ultrafast discharge/charge rate and robust cycle life for high-performance energy storage using ultrafine nanocrystals on the binder-free porous graphene foam[J]. Advanced Functionals Materials, 2016, 26(28): 5139-5148.

[141] Zhu Y, Chen Y, Chen J, et al. Lattice engineering on Li_2CO_3-based sacrificial cathode prelithiation agent for improving the energy density of Li-ion battery full-cell[J]. Advanced Materials, 2024, 36(13): 2312159.

[142] Zeng J, Wang T, Gu X, et al. Nickel-templated carbon foam anodes for sodium-ion batteries[J]. FlatChem, 2023, 40: 100508.

[143] Zhao J, Zhang Y, Chen J, et al. Codoped holey graphene aerogel by selective etching for high-performance sodium-ion storage[J]. Advanced Energy Materials, 2020, 10(18): 2000099.

[144] Tian H, Jia Y, Wang Y, et al. Graphene aerogel armed 3D ordered mesoporous carbon as versatile anode platforms for sodium-ion storage devices[J]. Advanced Functional Materials, 2024, 34(42): 2406827.

[145] Wang Q, Wang Y, Zeng J, et al. Zinc-guided 3D graphene bulk materials for high-performance binder-free anodes of potassium-ion batteries[J]. Journal of Power Sources, 2022, 540: 231613.

[146] Wang Y, Zeng J, Wang Y, et al. Biomass-derived carbon with large interlayer spacing for anode of potassium ion batteries[J]. Advanced Materials, 2024, 36(52): 2410132.

[147] Yang W, Zhou J, Wang S, et al. A three-dimensional carbon framework constructed by N/S Co-doped graphene nanosheets with expanded interlayer spacing facilitates potassium ion storage[J]. ACS Energy Letters, 2020, 5(5): 1653-661.

[148] Cheng Z, Chen Y, Lian J, et al. Interface engineering of MOF nanosheets or accelerated redox kinetics in lithium-sulfur batteries[J]. Angewandte Chemie International Edition, 2025, 64(11): e202421726

[149] Cheng Z, Lian J, Chen Y, et al. Robust In-Zr metal-organic framework nanosheets as ultrathin interlayer toward high-rate and long-cycle lithium-sulfur batteries[J]. CCS Chemistry, 2024, 6(4): 988-998.

[150] Cheng Z, Lian J, Zhang J, et al. Pristine MOF materials for separator application in lithium-sulfur battery[J]. Advanced Science, 2024, 11(31): 2404834.

[151] Wang M, Tan S, Kan S, et al. In-situ assembly of TiO_2 with high exposure of (001) facets on three-dimensional porous graphene aerogel for lithium-sulfur battery[J]. Journal of Energy Chemistry, 2020, 49: 316-322.

[152] Ye Z, Jiang Y, Yang T, et al. Engineering catalytic CoSe-ZnSe heterojunctions anchored on graphene aerogels for bidirectional sulfur conversion reactions[J]. Advanced Science, 2022, 9(1): 2103456.

[153] Zhai S, Ye Z, Liu R, et al. Defect strategy-regulated $MoSe_2$-modified self-supporting graphene aerogels serving as both cathode and interlayer of lithium-sulfur batteries[J]. Advanced Functional Materials, 2023, 34(17): 2314379.

[154] Qin L, Zhai D, Lv W, et al. Dense graphene monolith oxygen cathodes for ultrahigh volumetric energy densities[J]. Energy Storage Materials, 2017, 9: 134-139.

[155] Lacey S, Kirsch D, Li Y, et al. Extrusion-based 3D printing of

hierarchically porous advanced battery electrodes[J]. Advanced Materials, 2018, 30(12): 1705651.

[156] Cheng Z, Fang Y, Yang Y, et al. Hydrogen-bonded organic framework to upgrade cycling stability and rate capability of Li-CO_2 batteries[J]. Angewandte Chemie International Edition, 2023, 62(45): 202311480.

[157] Cheng Z, Wu Z, Chen J, et al. Mo_2N-ZrO_2 heterostructure engineering in freestanding carbon nanofibers for upgrading cycling stability and energy efficiency of Li-CO_2 batteries[J]. Small, 2023, 19(28): 2301685.

[158] Lin X, Wu Z, Xu C, et al. MOF Nanosheet enable accelerated redox kinetics and ultralow overpotential for light-assisted Li-CO_2 battery[J]. Small, 2025, 21(10): 2411559.

[159] Hu C, Gong L, Xiao Y, et al. High-performance, long-Life, rechargeable Li-CO_2 batteries based on a 3D holey rraphene cathode implanted with single iron atoms[J]. Advanced Materials, 2020, 32(16): 1907436.

[160] Zhou S, Qin J, Zhao X, et al. 3D hierarchically macro-/mesoporous graphene frameworks enriched with pyridinic-nitrogen-cobalt active sites as efficient reversible oxygen electrocatalysts for rechargeable zinc-air batteries[J]. Chinese Journal of Catalysis, 2021, 42(4): 571-582.

[161] Hu S, Han T, Lin C, et al. Enhanced electrocatalysis via 3D graphene aerogel engineered with a silver nanowire network for ultrahigh-rate zinc-air batteries[J]. Advanced Functional Materials, 2017, 27(18): 1700041.

[162] Lv X, Tian W, Yuan Z, Recent advances in high-efficiency electrocatalytic water splitting systems[J]. Electrochemical Energy Reviews, 2023, 6 (1) : 23.

[163] You B, Sun Y, Innovative strategies for electrocatalytic water splitting[J]. Accounts of Chemical Research, 2018, 51 (7) : 1571-1580.

[164] Shi L, Cui L, Ji Y, et al. Towards high-performance electrocatalysts: Activity optimization strategy of 2D MXenes-based nanomaterials for water-splitting[J]. Coordination Chemistry Reviews, 2022, 469: 214668.

[165] Yuan Y, Li X, Sun X, et al. Recent advances in functionalizing ZIFs and their derived carbon materials towards electrocatalytic water splitting[J]. Nano Energy, 2025, 136: 110727.

[166] Peng M, Shi D, Sun Y, et al. 3D printed mechanically robust graphene/CNT electrodes for highly efficient overall water splitting[J]. Advanced Materials, 2020, 32(23): 1908201.

[167] Luo H, Gao H, Zhang X, et al. Caterpillar-like 3D graphene nanoscrolls@CNTs hybrids decorated with Co-doped $MoSe_2$ nanosheets for electrocatalytic hydrogen evolution[J]. Journal of Materials Science and Technology, 2023, 136: 43-53.

[168] Zhu Y, Ran J, Qiao S, Scalable self-supported graphene foam for high-performance electrocatalytic oxygen evolution[J]. ACS Applied Materials and Interfaces, 2017, 9 (48) : 41980-41987.

[169] Zhang P, Chen L, Ge L, et al. A 3D rGO-supported $NiFe_2O_4$ heterostructure from sacrificial polymer-assisted exfoliation of NiFe-LDH for efficient oxygen evolution reaction[J]. Carbon, 2022, 200: 422-429.

[170] Zhang J, Jiang W, Niu S, et al. Organic small molecule activates transition metal foam for efficient oxygen evolution reaction[J]. Advanced Materials, 2020, 32(11): 1906015.

[171] Zhao L, Sui X, Li J, et al. Supramolecular assembly promoted synthesis of three-dimensional nitrogen doped graphene frameworks as efficient electrocatalyst for oxygen reduction reaction and methanol electrooxidation[J]. Applied Catalysis B: Environmental, 2018, 231: 224-233.

[172] Zhou H, Yang T, Kou Z, et al. Negative pressure pyrolysis induced highly accessible single sites dispersed on 3D graphene frameworks for enhanced oxygen reduction[J]. Angewandte Chemie International Edition, 2020, 59(46): 20465-20469.

[173] Zhou Y, Yang W, Utetiwabo W, et al. Revealing of active sites and catalytic mechanism in N-coordinated Fe, Ni dual-doped carbon with superior acidic oxygen reduction than single-atom catalyst[J]. Journal of Physical Chemistry Letters, 2020, 11(4): 1404-1410.

[174] Huang J, Lu Q, Ma X, et al. Bio-inspired FeN_5 moieties anchored on a three-dimensional graphene aerogel to improve oxygen reduction catalytic performance[J]. Journal of Materials Chemistry A, 2018, 6(38): 18488-18497.

[175] Choi J, Kim J, Wagner P, et al. Energy efficient electrochemical reduction of CO_2 to CO using a three-dimensional porphyrin/graphene hydrogel[J]. Energy & Environmental Science, 2019, 12(2): 747-755.

[176] Ma Z, Tsounis C, Kumar P, et al. Enhanced electrochemical CO_2 reduction of Cu@Cu_xO nanoparticles decorated on 3D vertical graphene with intrinsic sp^3-type defect[J]. Advanced Functional Materials, 2020, 30(24): 1910118.

[177] Yap F, Loh J, Yuan S, et al. Revolutionizing CO_2-to-C_2 conversion: unleashing the potential of CeO_2 nanocores for self-supported electrocatalysts with Cu_2O nanoflakes on 3D graphene aerogel[J]. Advanced Functional Materials, 2024, 35(3): 2407605.

[178] Lv K, Fan Y, Zhu Y, et al. Elastic Ag-anchored N-doped graphene/carbon foam for the selective electrochemical reduction of carbon dioxide to ethanol[J]. Journal of Materials Chemistry A, 2018, 6(12): 5025-5031.